POLITECNICO DI TORINO

Master degree course in Aerospace Engineering

Master Degree Thesis

Preliminary design and characterization of a Flight Control System for a Mach 5 aircraft

Supervisors
D. Ferretto
N. Viola
R. Fusaro
O. Gori

Candidate
Simona Loccisano

Academic Year 2022-2023

Abstract

The flight control system is an essential part of the aircraft because it allows to maneuver and trim the plane in all flight conditions, and considering this system in the preliminary stages of a project is important, especially in the design of high-speed vehicles. Indeed, in these cases the impact of control surfaces deflections on the aerodynamic performance may be very significant, and the ability to maneuver and trim the aircraft ensuring compliance with adequate stability requirements, is generally more difficult than the case of a conventional subsonic plane, mainly because high-speed vehicles must fly in very different flight regimes through their mission profile.

This thesis deals with the preliminary design of the flight control system of a supersonic aircraft. In particular, the concept of vehicle considered is the STRATOFLY MR5 that is a Mach 5 civil passenger aircraft, designed in the sphere of the H2020 MORE&LESS (MDO and Regulations for Low boom and Environmentally Sustainable Supersonic aviation) project, which receives funding from the European Commission. The steps followed in the design of the flight control system are shown in this thesis. Firstly, all control surfaces are geometrically defined, then possible deflections required in some reference trim conditions are estimated in order to evaluate the actuation powers, which allow to have an idea of the actuators necessary on board.

At the beginning of this thesis work, few data related to the MR5 concept of vehicle were available, thus some simplifying assumptions are made regarding for example the aerodynamic characteristics, stability, and trim analysis. These are necessary to proceed in the purpose of this thesis that consists in the preliminary characterization of a flight control system for the STRATOFLY MR5.

Contents

List of Figures

List of Tables

List of Symbols

α_{trim} Trim angle of attack $[deg]$

β Compressibility factor $\sqrt{|M^2 - 1|}$

δ_{BF} Deflection of body-flap $[deg]$

δ_{canard} Deflection of canard $[deg]$

δ_{elevon} Deflection of elevon $[deg]$

δ_{rud} Deflection of rudder $[deg]$

ϵ_{SKIN} Surface emissivity

$\frac{L}{D}$ Aerodynamic efficiency

$\frac{s}{l}$ Slenderness ratio= $\frac{Winghalfspan}{Totallengthofaircraft}$

Γ_V Dihedral angle of V-tail $[deg]$

Λ_{wing} Wing leading-edge sweep angle $[deg]$

Λ_c Canard sweep angle $[deg]$

λ_c Taper ratio of canard

Λ_V Sweep angle of V-tail (single surface) $[deg]$

λ_V Taper ratio of V-tail

λ_{rud} Taper ratio of rudder

μ Air coefficient of viscosity $[Pa \cdot s]$

ρ Air density $[kg/m^3]$

ρ_{SL} Air density at sea level $[kg/m^3]$

a Speed of sound $[m/s]$

AR_c Aspect ratio of canard

AR_V Aspect ratio of V-tail

b Wingspan

b_c Span of canard $[m]$

b_V Span of V-tail (single surface) $[m]$

b_{elevon} Span of elevon $[m]$

$b_{M_{BF}}$ Major span of body-flap $[m]$

$b_{m_{BF}}$ Minor span of body-flap $[m]$

C_1 Coefficient multiplying $sin\alpha$ in C_L expression

C_2 Coefficient multiplying $sin^2\alpha$ in C_L expression

C_D Drag coefficient

C_L Lift coefficient

C_{D_0VT} Zero-lift V-tail drag

C_{D_0} Zero-lift body drag

C_{D_i} Induced drag

$C_{D_{BB}}$ Bluntness drag coefficient for body

$C_{D_{FB}}$ Friction drag coefficient for body

$C_{D_{PB}}$ Pressure drag coefficient for body

c_{elevon} Chord of elevon $[m]$

$c_{h_{surface}}$ Hinge arm of mobile surface $[m]$

C_{L_0} Lift coefficient at zero angle of attack

C_{M_h} Hinge moment coefficient

C_{M_y} Pitching moment coefficient

$c_{M_{rud}}$ Major chord of rudder $[m]$

$c_{m_{rud}}$ Minor chord of rudder $[m]$

c_{r_c} Root chord of canard $[m]$

c_{r_V} Root chord of V-tail $[m]$

c_{t_c} Tip chord of canard $[m]$

c_{t_V} Tip chord of V-tail $[m]$

D Drag force $[N]$

h_{cruise} Cruise altitude $[m]$

H_{rud} Height of rudder $[m]$

K_a Coefficient multiplying $\alpha°$ in C_{M_h} expression

K_b Coefficient multiplying $\delta°$ in C_{M_h} expression

L Lift force $[N]$

l_c Moment arm of canard $[m]$

L_{BF} Axial length of body-flap $[m]$

l_{ref} Total length $[m]$

l_{V-tail} Moment arm of V-tail $[m]$

M Mach number

M_y Pitching moment $[Nm]$

$M_{actuator}$ Actuator mass $[kg]$

M_{cruise} Cruise Mach number

M_{hinge} Hinge moment of mobile surface $[Nm]$

M_{y_T} Contribution of thrust to pitching moment $[Nm]$

P Actuation power $[W]$

r_{NOSE} Nose radius $[m]$

Re_b Reynolds number for body

S_π Maximum cross-sectional area $[m^2]$

S_c Plan area of canard $[m^2]$

S_V Area of V-tail (single surface) $[m^2]$

S_{BF} Area of body-flap (single surface) $[m^2]$

S_{elevon} Area of elevon (single surface) $[m^2]$

S_{ref} Total plan area of aircraft $[m^2]$

S_{rud} Area of rudder (single surface) $[m^2]$

$S_{t_{BF}}$ Total area of body-flaps $[m^2]$

$S_{t_{elevon}}$ Total area of elevons $[m^2]$

S_{trud} Total area of rudders $[m^2]$

S_{tV} Area of both V-tail sections $[m^2]$

S_{wet} Wetted area of aircraft $[m^2]$

T Thrust $[N]$

t Atuation Time $[sec]$

T_{cruise} Air temperature at cruise altitude $[K]$

T_{LE} Leading-edge radiation equilibrium temperature $[K]$

V_c Canard volume coefficient

V_{V-tail} V-tail volume coefficient

W Weight of aircraft $[N]$

x_{ac} Aerodynamic center position $[m]$

x_{GC} Center of gravity position $[m]$

x_{SM} Static margin$=x_{GC} - x_{ac}$

AoA Angle of Attack

AR Aspect ratio, $\frac{b^2}{S_{ref}}$

ARV Ascent and Re-entry Vehicle

ATR Air-Turbo-Rocket

CAV Cruise and Acceleration Vehicle

CCD Climb, Cruise and Descend cycle

CoG Center of Gravity

DMR Dual Mode Ramjet

FCS Flight Control System

LTO Landing and Take-Off cycle

MAC Mean Aerodynamic Chord $[m]$

RV-NW Non Winged Re-entry Vehicle

RV-W Winged Re-entry Vehicle

SSTO Single-Stage-To-Orbit system

TSTO Two-Stage-To-Orbit system

Chapter 1

Introduction to FCS and high-speed aircraft

1.1 Flight control system

The flight control system includes all necessary devices to control the plane in flight, ensuring precision, stability, and the alleviation of pilot workload. The maneuvers and attitude control are guaranteed by moving the control surfaces that do not constitute alone the FCS. This also comprises the actuation system that allows to convert an input into a surface displacement and all it takes to define a flight command. Therefore, the preliminary design of the flight control system involves two parts: the configuration and the architecture of the system. [1]

The configuration includes all flight control devices that, in a conventional aircraft can be distinguish between primary and secondary. In particular, the primary surfaces consist of elevators for pitch, ailerons for roll, and rudders for yaw, and they are continuously activated to maintain safe attitude and trajectory control of the aircraft. While secondary surfaces usually include high lift devices and spoilers, and they are displayed intermittently or only during certain flight phases, and thus less critically for a safe flight. All these mobile surfaces contribute also to lateral, longitudinal, and directional trim of the aircraft.

In addition to trim and controllability of the aircraft, another important feature is the stability, that depends on different aspects such as the position of gravity and pressure centers, and the presence of stabilization devices like horizontal and vertical tails. If the stability requirements are not met, modern active control systems should be introduced. Trim, controllability, and stability are also interdependent with each other.

The FCS architecture includes instead the actuation system, it is defined in terms of number of actuators, distribution of the power supply and flight control computers. As reported in reference [1] its design is primary driven by safety considerations, for example it must be ensure that the complete loss of power supply for the flight control actuation systems should be extremely improbable (10^{-9}). From this point of view the fault tolerance and fault detection are two very useful tools.

In early aircraft and currently in small ones, the actuation flight control system used is mechanical. This uses mechanical parts such as cables, pulleys, chains to transmit the pilot's command directly to the control surfaces or to some valves connected to hydraulic actuators that finally move the surfaces. However, modern, and sophisticated aircraft are equipped with fly-by-wire flight control system with stringent requirements in terms of safety, availability, and reliability. It replaces most of the mechanical connections between pilot controls and surfaces with an electrical interface. This system has many advantages such as flight envelope protection rejecting pilot commands that might exceed admissible values of speed, load factors, and attitude, weight and maintenance reduction, the possibility to implement more complex control laws, increase stability and ensure the required handling qualities.

Therefore, as we can see in the flowchart of figure 1.1, the preliminary design of a FCS generally starts with the geometrical definition of all control surfaces and their deflections, and it proceeds with the estimate of hinge moments and actuation power of the mobile surfaces, the actuation system sizing, and the flight control system architecture definition.

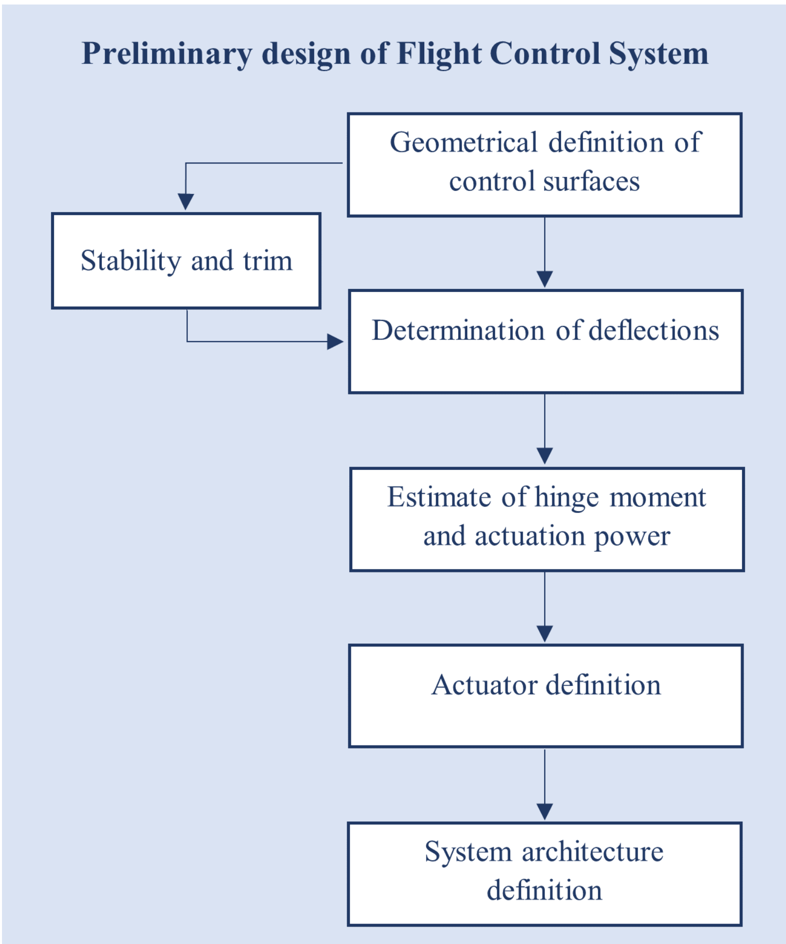

Figure 1.1: Preliminary design of FCS

1.2 High-speed aircraft

The high-speed aircraft are systems capable of flying faster than the speed of sound, they are divided into supersonic vehicles up to Mach 5 and hypersonic ones with higher values of Mach. There is a great interest in these types of aircraft that allow to reduce significantly flight times, but at the same time their design is characterized by more challenges than the conventional subsonic planes.

As it can be seen in figure 1.2, the global supersonic and hypersonic aircraft market was valued at about $4,1 billion in 2021, and it is expected to reach $5.4 billion by 2032 [13]. Therefore, it can be noted that there is a great interest in these aircraft categories. The growing demand is, as always, mainly linked to military applications, thus to the defence industry of various nations, for example there is an increasing number of modernization programs to replace aging 4th generation fighters with newer platforms. However, this market growth is also due to a greater interest in the last decade for civil applications by startups and emerging players. As regards the speed regime the market is expected to be dominated by the demand for supersonic aircraft in the period considered because the hypersonic technology is still not sufficiently known and advanced compared to the supersonic one, which already has an important operational history both in commercial and military aviation. [13]

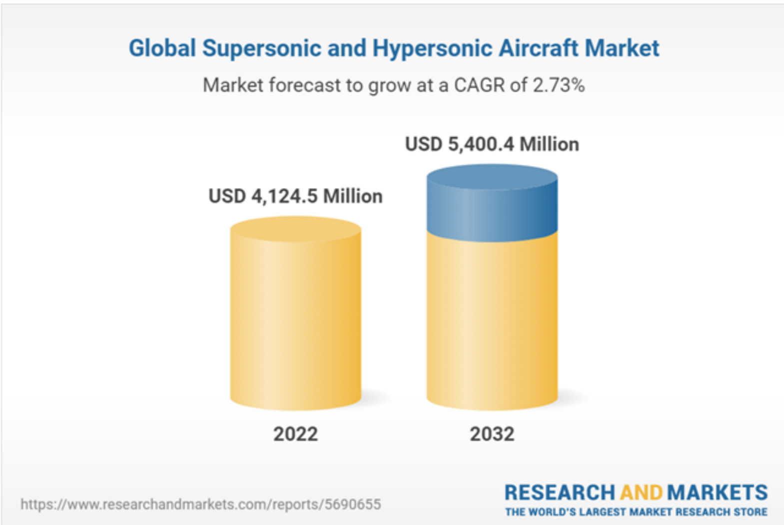

Figure 1.2: Global Supersonic and Hypersonic aircraft market. (Source: [13])

1.2.1 Brief overview of high-speed aircraft

Supersonic vehicles

The first supersonic aircraft was the Bell-X1, which reached Mach 1.06 overcoming the sound barrier for the first time in 1947. It was a rocket-engine powered aircraft belonging to the series of the X-planes, i.e., experimental United States aircraft used to test and evaluate new technologies. Since then, several research has been made in the high-speed field, and various increasingly technologically advanced projects have been born, which have mainly led to experimental or military aircraft. A summary of the supersonic aircraft progress can be seen in figure 1.3, taken from reference [14]. There have been only two supersonic civil aircraft that both achieved Mach 2, i.e., the Russian Tupolev Tu-144, which officially became the first supersonic commercial transport aircraft in 1970 and was retired from passenger service in 1978, and the British/French Concorde, which entered officially in service in 1976 and was retired in 2003.

Today it seems that the return to supersonic civil transport is possible, two examples of aircraft, currently being worked on, are the Spike S-512 (see figure 1.4) and the Overture (see figure 1.5). The first is a business jet flying at Mach 1.6, carrying 12 to 18 passengers and it is designed by the Spike aerospace [15], while the second is an airliner cruising at Mach 1.7 with a passenger capacity of 65 to 80, and it is being made by Boom supersonic [16], which has foreseen the release into service by 2029.

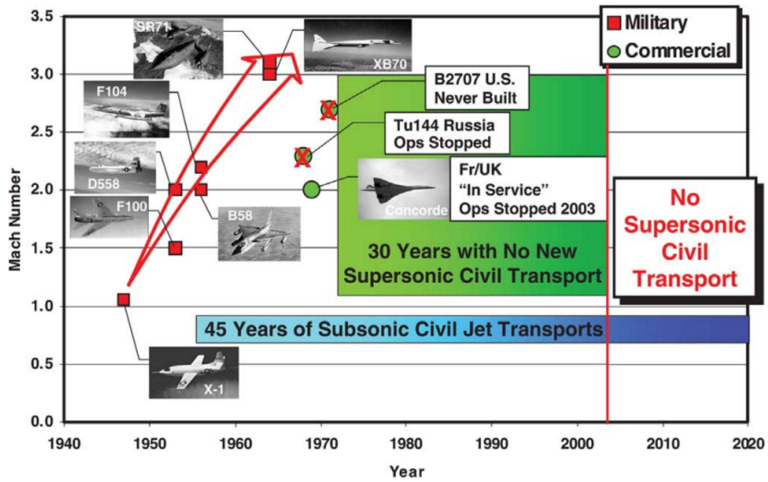

Figure 1.3: Supersonic aircraft progress. (Source: [14])

Figure 1.4: Spike S-512

Figure 1.5: Overture

Hypersonic vehicles

Hypersonic vehicles are devices that reach speed higher than Mach 5. These systems can be divided into three categories: winged re-entry vehicle (RV-W), non-winged re-entry vehicle (RV-NW), and airbreathing cruise and acceleration vehicle (CAV). [17]

- Winged re-entry vehicles are launched vertically typically by means of rocket boosters, but they can also be the rocket-propelled upper stages of two-stage-to-orbit (TSTO) systems, and in this case, they are launched horizontally. These vehicles cover a speed range from Mach 30 to 0. The only one of these vehicles to have been operational is the Space Shuttle Orbiter (fig.1.6a), which was launched into orbit for the first time in 1981 and completed its last mission in 2011. The others are mainly conceptual studies or projects such as the HOPE-X (fig.1.6b), which was a Japanese experimental spaceplane project, started in 1980's and cancelled in 2003. Today a vehicle that is being worked on is the Boeing X-37B (fig.1.6c), also called Orbital Test Vehicle (OTV), which is an unmanned experimental spaceplane, whose first flight into space dates to 2010 and so far, it has completed 6 successful missions.

- Non-winged re-entry vehicles are the space capsules, which return to Earth after a spaceflight and cover a speed range from Mach 30 to 0. Some examples (see fig.1.7) belonging to this category are: OREX, APOLLO, ARD, SOYUZ, Dragon2.

- Airbreathing cruise and acceleration vehicles are aircraft that operate entirely in the atmosphere. In this category there are the airbreathing accelerators for space transportation purposes, as the first stage of a TSTO system, which departs from the point A and returns to the same point, and also the airbreathing cruisers for transportation purposes, flying from a starting point A to the destination B. They cover a speed range from Mach 0 to 7 (or 12). Compared to the other two categories, considerable flight experience is not available, and the technological maturity of these aircraft is lower. Some examples of hypersonic CAVs (see fig.1.8) are: the first stage of the TSTO Saenger system, the Boeing X-51 Waverider, the STRATOFLY MR3.

It is noted that a fourth category of ascent and re-entry vehicles (ARV) can be defined, they are single-stage-to-orbit (SSTO) space transportation systems with airbreathing and rocket propulsion. The problems of these vehicles are a mixture of the problems encountered for RV-Ws and CAVs [17].

(a) *Space Shuttle Orbiter* (b) *HOPE-X* (c) *Boeing X-37b*

Figure 1.6: Examples of RV-W

(a) *APOLLO* (b) *SOYUZ* (c) *Dragon2*

Figure 1.7: Examples of RV-NW

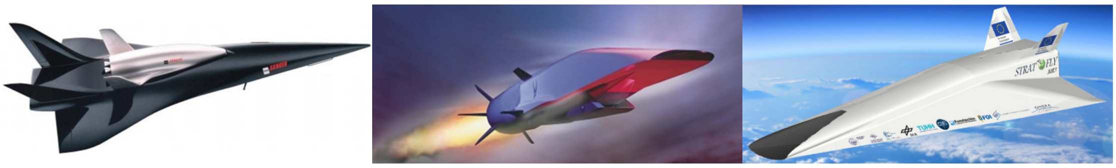

(a) *TSTO Saenger system* (b) *Boeing X-51 waverider* (c) *STRATOFLY MR3*

Figure 1.8: Examples of CAV

Each of these categories has different problems and characteristics related to the mission requirements and the operating environment that must be considered in the design phases. For example, in the CAV category the ability to carry out an efficient cruise is very important for the hypersonic passenger transport aircraft because it allows to reduce fuel consumption and increase the range, thus in the cruise phase high aerodynamic efficiency (L/D) is required. This is usually obtained using slender configurations that operate at small angles of attack. On the contrary, the winged re-entry vehicles are required to maximize their deceleration capability for re-entry missions, thus they are usually characterized by blunt shapes that operate at large angles of attack with the aim to maximize their wave drag due to volume and viscous drag due to separation.

In this thesis work the case study considered is a civil passenger aircraft flying at Mach 5 in cruise. It falls into the category of airbreathing cruise and acceleration vehicles, and as regards the speed regime it is on the border between the supersonic and hypersonic classification.

Some aspects of this category of supersonic and hypersonic CAV aircraft are reported below.

1.2.2 Typical aspects of supersonic and hypersonic CAV

Aerodynamics

The aerodynamics of high-speed aircraft is very complex. They are designed to operate their cruise at a specific high speed, but they must fly in different flight regimes to reach the desired conditions. This consideration is important because the aerodynamic behavior, stability and control of the vehicle can change drastically passing from a regime to another and the configuration that is optimal for example for the hypersonic cruise, is not suitable for the first subsonic phases of the mission. Even subsonic aircrafts experience this phenomenon, but it is much more important when the speed range is so large.

The choice of the configuration is largely driven by mission requirements as mentioned before, an important aim for CAVs is to carry out a cruise as efficient as possible, with high aerodynamic efficiency (L/D) that allows to maximize the range. For this reason, the drag (D) that envelops in flight must be minimized. The main contributions of drag are friction drag, drag due to lift and wave drag. The latter is caused by the occurrence of shock waves that specifically affect the high-speed flight regimes, and they arise at speed exceeding the critical Mach number. The wave drag depends on the Mach number, the shape of the vehicle, and the angle of attack, and in order to minimize it, slender vehicles with sharp leading edge operating at small angles of attack are required, in particular at hypersonic Mach number the slenderness ratio (s/l) of swept wings, defined as the ratio between the wing half span and the total length of the aircraft, should be lower than 0.3 [17].

Another important aspect to consider is the propulsion system integration, which largely affects the slenderness of the entire vehicle. The size of this is mainly driven by the necessary capture area of the inlet and by the exhaust nozzles, which both generally increase as the cruise Mach number rises. Furthermore, the big dimensions of these elements required at high speed tend to negatively affect the performance in transonic regime because in this flight condition the air intakes and nozzles are much larger than those necessary to reach the required thrust, thus they cause an increase in drag and then the nozzles are usually overexpanded because the altitudes are lower than the cruise one so the air pressure is greater. This is an example of the problem mentioned before, related to the fact that the requirements required in the various flight regimes, which can be crossed along the mission profile, can be very different, thus it is important to find the best compromise.

Considering what has been said, the waverider configuration seems to be very promising for high supersonic and hypersonic aircraft. It is a non-traditional aerodynamic shape that allows to reach high aerodynamic efficiency with relatively large inner volumes, thanks to positive effects of airframe-powerplant integration [18].

A waverider is a supersonic or hypersonic lifting body, characterized by attached, or nearly attached, bow shock wave along its leading edge. In addition to achieving high aerodynamic efficiency compared to other conventional configurations, it has another advantage, i.e. it guarantees an ideal precompression surface of the inlet system. [19]

It is noted that this type of configuration also characterizes the case study considered in this thesis work.

Propulsion system

The propulsion system of high-speed aircraft is another aspect characterized by more challenges than the conventional subsonic aircraft. The difficulty linked to the integration of this system, whose sizes tend to increase as the required Mach number rises, with the aerodynamic configuration of the entire aircraft has been already mentioned before.

Another challenge consists in the type of engines that often have to be combined to reach the desired high speeds. Ramjet and/or scramjet engines are usually used to fly at supersonic or hypersonic velocities up to about Mach 12. However the take-off is not possible with these engines because they can operate only from a certain speed, thus a turbojet propulsion is required for low Mach numbers, while a rocket propulsion is needed to reach speeds higher than those indicated before. Today there are also alternative engines, in which combined cycles are applied. The aim is to combine the positive aspects of turbojet engines with rocket engines or other air-breathing cycles such as ramjet and scramjet, which allows to obtain air-breathing engines that can operate at higher Mach numbers and altitudes than the simple turbojets.

An important additional consideration is about the aerodynamic and propulsive forces that are strongly coupled. In general, the speed vector could change in magnitude and direction in a considerable range depending on flight speed, angle of attack and power setting of the propulsion system [17], for example when switching from using one engine type to another, and this aspect can play a significant role in the stability and trim of the aircraft.

High heat flux and structural temperature

Another important problem that characterized high-speed aircraft consists of the high heat fluxes and temperatures on the surface. This problem gets worse as the speed increases, and it is mainly due to the skin friction drag. In particular, downstream of the leading-edge shock waves, a boundary layer is created on the surface with strong viscous dissipations that generate high temperatures. Furthermore, different problems occur depending on the speed, for example in supersonic flight regimes the vibrational excitation effects tend to prevail, while as the speed increases especially in hypersonic regimes, the vibrational energy of the molecules becomes significant and the phenomenon of the molecule's dissociation begins to occur, increasing the reactivity of the atmospheric gas.

As regards the temperatures, the most critical points are the leading edges where the highest values are recorded. For example an aircraft flying at Mach 5 can reach maximum temperatures in these critical points of around 1100°C and average temperatures around 400-450°C. These values depend on several factors such as speed, altitude, atmospheric conditions but also geometric characteristics of the configuration. For example, the sharp leading edges of the slender configurations that characterize CAV aircraft are not helpful because they have a very small radius of curvature, and the heat flux results to be inversely proportional to the square root of the leading edge radius.

Therefore, it is very important the choice of appropriate materials that can be used at high temperatures or the application of a thermal protection system that is not required in a conventional subsonic aircraft.

FCS

Some critical aspects must be considered also regarding the flight control system. For example, high-speed aircrafts have generally the same control surfaces of the ordinary ones that are elevators, ailerons, and rudders but there are some differences, such as the possible presence of multi-functional control surfaces and the lack of the horizontal tail. This last one is increasingly common as Mach increases. Some reasons are the large thermal loads, that are difficult to dissipate, the weight increase, problems with the propulsion integration, and the low stability contribution because these surfaces and their moment arm are usually small.

Another important aspect is the impact of control surfaces deflections on the aerodynamic performance of the aircraft. This is usually neglected in the early stage of conventional subsonic aircraft design, but it is not acceptable for hypersonic vehicles that can experience a reduction of about 30% of their maximum theoretical efficiency due to the control surfaces deflections. [2]

Furthermore, the control surfaces, as mentioned before, are necessary to maneuver and trim the aircraft in every flight condition. These capabilities, and the stability of the vehicle, are much influenced by the positions of center of gravity and aerodynamic center. In general, it is more difficult to maneuver a very stable aircraft, which has a center of gravity much further forward than the aerodynamic center, because the moment arm of the wing lift result big, and as consequence greater forces by the control surfaces are necessary to balance the aircraft; therefore, maneuvers with considerable efforts and with greater surface deflections are needed. This is generally true for every aircraft but in the design of high-speed systems the analyzes to done are more complex because across the mission profile the position of these two important points can change very significantly. The shift of the center of gravity is influenced a lot by the big quantities of fuel that these aircrafts consume and that cause important changes in the distribution of the masses, while the position of the aerodynamic center varies according to the different flight regimes, from low to high speed. From these considerations it is possible to note the importance of a high integration between on-board subsystem, which is another typical aspect of high-speed vehicles [2]. In this case, it may be useful act upon the fuel system to control the center of gravity shift, and upon the avionic system, in which an appropriate active control system can be implemented to solve stability problems and guarantee desirable flight qualities over a large flight envelope [3].

Environmental impact

The environmental impact of aviation refers to the effects on the natural environment due to the combustion products and noise. It is possible to distinguish three different problems, which are the air quality impact, the climate impact and the noise associated with aircraft. The first two are related to engine emissions that typically include nitrogen oxides (NO_x), unburnt hydrocarbons (HC), water vapour, carbon monoxide (CO), particulates and more. In particular, the air quality is associated especially to the noxious emissions released in the low altitude flight phases that constitute the so-called Landing and Take-Off cycle (LTO), while the climate impact is affected especially by the emissions released at the high altitudes of the so-called Climb, Cruise and Descend cycle (CCD). A distinction between the flight phases can be made also for the noise problem.

In general, the problem of environmental impact affects all subsonic, supersonic, and hypersonic aircraft, but the effects of high-speed vehicles are much more severe than the subsonic ones [20].

A first reason is linked to the propellant consumption of high-speed aircraft, which is much higher, so even if the engine used are characterized by low emission indices, the overall amount of emissions along the entire mission profile is greater.

Furthermore, high-speed aircraft operate at higher altitudes than the subsonic ones, mainly in the stratosphere above 20 km altitude. This leads to additional problems that cause greater effects on climate by these vehicles. For example, the emissions of NO_x, water vapour and aerosols lead to chemical reactions that cause changes in stratospheric ozone concentration. Another problem associated to the high altitude, in which some emissions are released, is about the residence times that increase in the stratosphere. This causes a greater accumulation over time of the species emitted, and thus a greater effect on climate. In particular, according to several studies H_2O emissions into the stratosphere represent the most important effect on climate by high-speed aircraft, and their importance increases as the cruising altitude rises [20].

A specific problem of high-speed aircraft relating instead to noise emission is the sonic boom. When a plane flies with a speed greater than the speed of sound, it generates a series of shock waves that at a great distance coalesce into two shock waves (see figure 1.9), one in the front of the aircraft and one in the rear part, called bow and tail shock waves. At the bow wave there is a compression that generates an increase in local pressure with respect to the atmospheric pressure, then there is an expansion, which leads to lower values with respect to the atmospheric pressure, followed by a recompression at the tail wave [21]. The portion of the ground that is affected by this wave system is defined as sonic boom carpet, and people or things that are inside this area are subjected to these pressure changes, which result in a loud noise. For these reasons aircraft can not fly at supersonic or hypersonic speed over land and populated area.

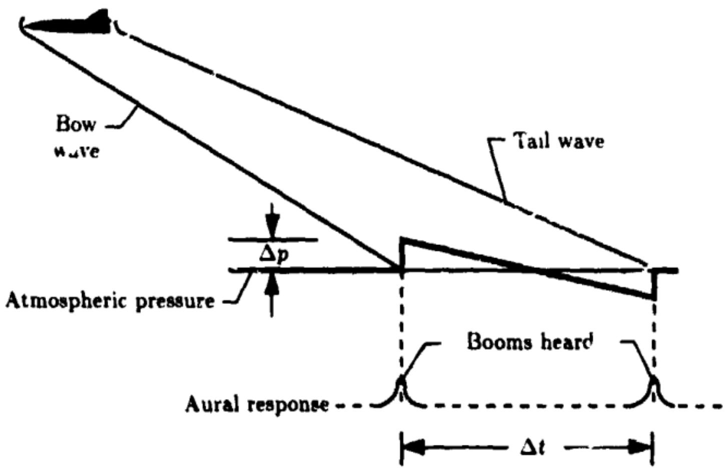

Figure 1.9: Far-field wave pattern (Source:[21])

As regards the regulatory issues the annex 16 to the Convention on International civil Aviation pertains to Environmental protection. In particular, the volume II contains standards and recommended practices (SARP) for aircraft engine emissions, and in detailed Chapter 3 is applicable to turbojet and turbofan engines for propulsion at supersonic speeds manufactured from 18 February 1982, while the Chapter 2 is applicable to engines of subsonic planes. The SARPs in Chapter 3 were developed in the age of Concorde, indeed in February 2007 the Committee on Aviation Environmental Protection (CAEP) reported that the requirements in Chapter 3 "were outdated and should not be applied to new engine projects" [20]. Furthermore, there is not currently a noise regulation applicable to new supersonic aircraft, except for the prohibition related to the sonic boom.

Therefore, it is evident that the engine emissions and noise regulations for high-speed aircraft needs to be updated, but for this purpose more data and a better comprehension of the environmental impact of supersonic aviation is necessary. In this context two projects funded by the European Commission, on supersonic aviation and environmental impact started in 2021, that are SENECA and MORE&LESS (MDO and Regulations for Low boom and Environmentally Sustainable Supersonic aviation) [20]. Finally, it is highlighted that the case study considered in this thesis work is part of this last project.

Chapter 2

Stratofly re-design: from Mach 8 to Mach 5

2.1 H2020 MORE&LESS project

Since the last civil supersonic flight of Concorde in 2003, several projects with the aim to revive high-speed travel have been proposed and continue to exist. Among these, there is also the STRATOFLY project [4], that has received funding from the European Union's Horizon 2020 research and innovation program, and studies the feasibility of high-speed passenger stratospheric flight. STRATOFLY MR3 (see figure 2.1) was designed to fly at Mach number of 8.

Now, the European Commission is funding another project called H2020 MORE&LESS (MDO and Regulations for Low boom and Environmentally Sustainable Supersonic aviation) [5], aiming at supporting Europe to shape global environmental regulations for future supersonic aviation. This project focuses on the entire spectrum of supersonic speed regime, ranging from Mach 2 to Mach 5, and on aircraft using not only hydrocarbon fuel but also alternative fuels such as biofuels and liquid hydrogen. A strategic step to reach the goal of MORE&LESS is to assess near and far-future supersonic aviation, selecting and analyzing a set of real up-to-date case studies. Among these there is the MR5 concept [6], that is a Mach 5 civil passenger aircraft. This concept has not been developed completely from scratch but by exploiting the results of the H2020 STRATOFLY project.

In the next sections, some information on the starting concept, the STRATOFLY MR3, and some aspects on the methodology used to re-design it to obtain the MR5, are provided.

2.2 STRATOFLY MR3

The STRATOFLY MR3 [2], [7], [8] is a highly integrated aircraft that reaches Mach 8 and can carry up to 300 passengers as payload. It features a waverider configuration that allows to maximize the aerodynamic efficiency (L/D) during the hypersonic cruise, the propulsive system is integrated at the top of the vehicle, and this aspect allows to maximize the available planform area for lift generation without additional drag penalties and to optimize the internal volumes. Six Air-Turbo-Rocket engines and one Dual-Mode-Ramjet engine constitute the propulsion system. This aircraft uses liquid hydrogen as propellant, to be stored in cryogenic integrated bubble tanks. The main advantage is the possibility to cover antipodal routes flying at Mach 8, thanks to the high specific energy of the liquid hydrogen, with the guarantee of no CO_2 emission.

Figure 2.1: STRATOFLY MR3

The STRATOFLY typical mission profile (see figure 2.2) allows to cover antipodal routes with a distance up to 19000 km in less than 3h, and it includes a starting subsonic climb that ends at an altitude of 11-13 km and at Mach 0,95, followed by a subsonic cruise necessary to prevent the sonic boom while flying over land. When the aircraft is about 400 km away from the departure airport, the supersonic climb starts, and it ends at Mach 4 and at an altitude of 30-32 km. In these phases the ATR engines are used, and they are switched off to activate the DMR engine that allows to accelerate from Mach 4 to Mach 8 during the hypersonic climb. The hypersonic cruise begins at Mach 8 and at an altitude of 32-35km, and at the end of it DMR engine is turned off and the vehicle performs a gliding descent.

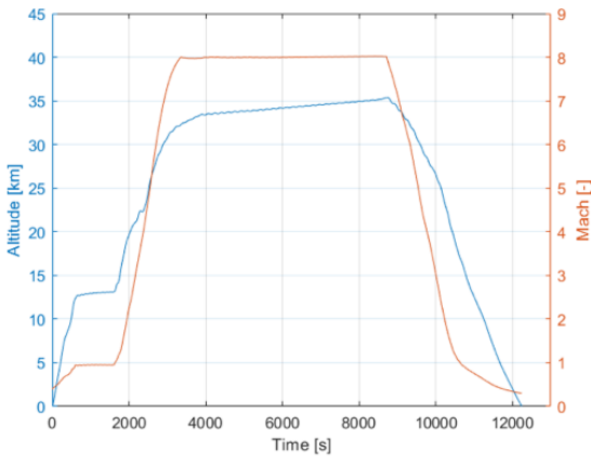

Figure 2.2: The STRATOFLY MR3 mission profile

In table 2.1 some data of STRATOFLY MR3 are reported.

Table 2.1: STRATOFLY MR3 data

Parameter	**Value**	**Unit of measure**
Length	94	[m]
Wingspan	41	[m]
Total plan area	2491	[m^2]
Wetted area	5422	[m^2]
Max passengers	300	-
GTO mass	400	[Mg]
Fuel mass	∼180	[Mg]
Available range	∼24000	[km]

2.3 STRATOFLY MR5

As previously mentioned, the MR5 concept is meant to be a civil passenger aircraft flying in cruise at Mach 5, to be used as case study for the analysis of the H2020 MORE&LESS project. The definition of this new concept, as reported in reference [6], can be obtained exploiting the results of the STRATOFLY MR3, that proved to be very efficient in terms of performance and operations at Mach 8.

In reference [6], the methodology used to re-design the aircraft is described in detail. Only some aspects are briefly introduced below, and the final results are reported, useful as a starting point for the preliminary design of the flight control system.

Firstly, the original configuration of MR3 was considered, it was designed to fly in cruise at Mach 8, thus it is also capable of carrying out an off-design mission with the cruise at Mach 5. In these conditions it presents reduced aerodynamic efficiency, unbalanced lifting surface, excessive volume and problem on the intake and nozzle sides. After these evaluations, a re-design of the original layout was considered necessary to improve the efficiency and the environmental sustainability for the new mission profile with Mach 5 cruise.

In the first stages of the re-design, the problems of the air intake spillage and of the uncorrected expansion in nozzle were analyzed, and a reduction of the original nozzle of about 20 m was considered as first result. Then, a low fidelity design and analysis methodology were used to investigate the performance and geometric characteristics of different intake designs. The length of the re-designed intake for MR5 was reduced by about 10 m. Considering these first results a scaling process appeared to be necessary with a total length reduction of about 30m

At the beginning two possible approaches were taken into account, the homogeneous scaling and the 1D scaling. With the first solution (see figure 2.3a), the original layout of MR3 remains unchanged with the same proportions but the overall dimensions are reduced. On one hand this is advantageous because aerodynamic performance indices are the same, but on the other hand some original problems of aerodynamic balance continue to exist.

On the contrary, the 1D scaling generates a different configuration with a reduced slenderness (see figure 2.3b) because the length is reduced at the same way with a scaling factor of 0.68, while the wingspan remains unchanged, but this scaled version appeared more promising in terms of aerodynamic balance, volume feasibility and range capability. So, it was decided to consider this configuration for the following steps.

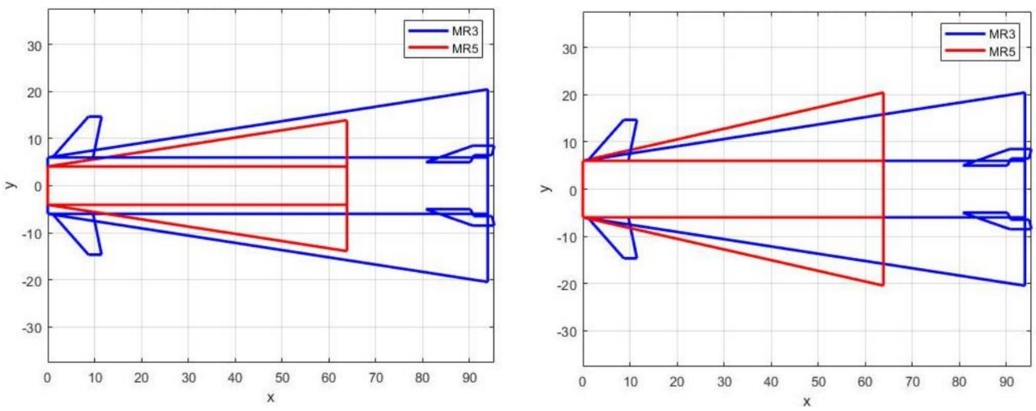

(a) *Homogeneous scaling* (b) *1D scaling*

Figure 2.3: MR5 scaling approaches

In figure 2.4 a possible mission profile with a cruise altitude of around 30 km and some data of the new MR5 configuration are reported.

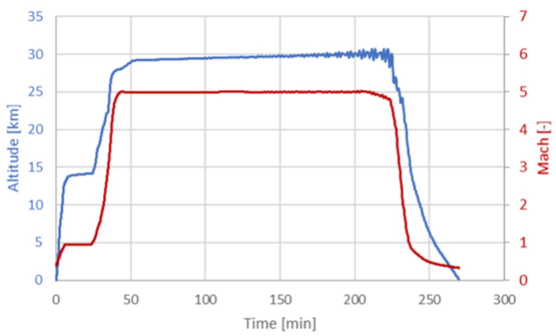

Parameter	**Value**	**UoM**
Length	64	[m]
Wingspan	41	[m]
Total plan area	1696	[m^2]
Wetted area	3710	[m^2]
Max passengers	∼200	-
GTO mass	275	[Mg]
Fuel mass	∼120	[Mg]
Available range	∼22500	[km]

Figure 2.4: Mission profile and data of STRATOFLY MR5

Chapter 3

Geometrical definition of control surfaces

3.1 Known starting data

As mentioned in the introduction chapter, the first step in the definition of the MR5's flight control system, consists in sizing the new control surfaces. It has been decided to keep the same configuration of the STRATOFLY MR3 (see figure 3.1) that includes 2 body flaps on the top of the integrated nozzle, 4 elevons, a fully movable canard and a V-tail with 2 rudders [2].

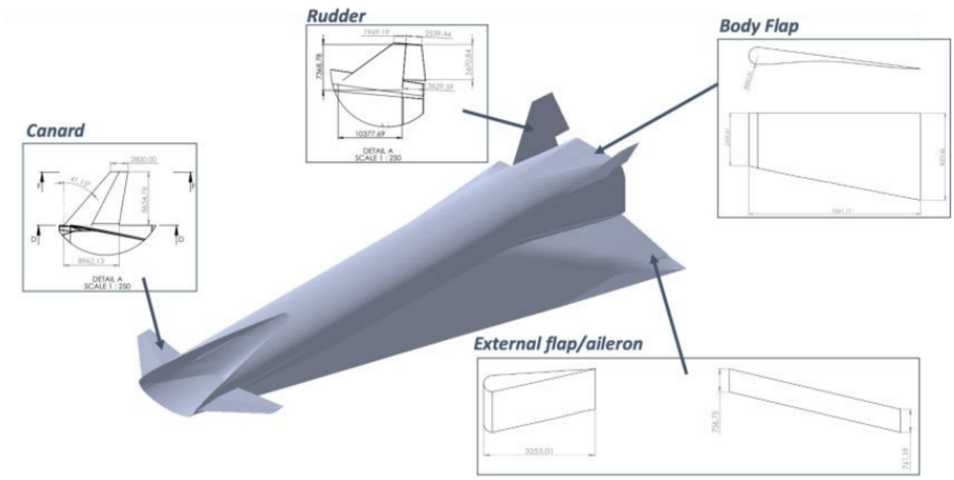

Figure 3.1: Control surfaces of STRATOFLY MR3

The new concept of aircraft MR5 was obtained applying a linear scaling of the MR3 configuration so scaling the respective control surfaces homogeneously is not correct because the overall proportions are different. Despite this, the known surfaces parameters of MR3 are a good starting point for the new sizing.

In tables 3.1, 3.2 and 3.3, the known starting data of the STRATOFLY MR3 and MR5 are reported.

Table 3.1: Geometric parameters of MR5

Parameter	**Value**	**Unit of measure**
S_{ref}	1696	$[m^2]$
l_{ref}	64	[m]
MAC	39	[m]

Table 3.2: Control surfaces of STRATOFLY MR3

External Elevon (single surface)	
Chord [m]	3
Span [m]	5
Maximum deflection [°]	+/-25
Surface $[m^2]$	15
Internal Elevon (single surface)	
Chord [m]	3
Span [m]	5
Maximum deflection [°]	+/-25
Surface $[m^2]$	15
Canard (single surface)	
Root chord [m]	8.7
Tip chord [m]	2.8
Span [m]	8.7
Maximum deflection [°]	+/-20
Sweep angle [°]	49
Surface $[m^2]$	50
Rudder (single surface)	
Major chord [m]	3.6
Minor chord [m]	2.5
Height [m]	6.5
Maximum deflection [°]	+/-20
Inclination [°]	33
Surface $[m^2]$	50
Body flap (single surface)	
Major span [m]	4.05
Minor span [m]	2.58
Length [m]	7.14
Maximum deflection [°]	-30
Surface $[m^2]$	23.7

Table 3.3: Geometric parameters of MR3

Parameter	Value	Unit of measure
S_{ref}	2491	$[m^2]$
l_{ref}	94	[m]
MAC	58	[m]
CoG	50	[m]

3.2 Canard

Initially, the configuration of MR3 was not equipped with canard. This has been added subsequently for trim-ability reasons [8], and it consists in a fully movable surface placed at the beginning of the structure.

For the sizing of this surface the volume coefficient is used, as indicated in the tail design method suggested by M. H. Sadraey [9]. It is a significant parameter for both longitudinal stability and trim, and it is representative of the pitching moment generated by the surface. This coefficient is calculated as the ratio of two numbers. In the numerator there are parameters related to the specific surface, that is the canard in this case, in particular the product between its plan surface and its moment arm, while in the denominator there are usually parameters related to the wing such as the product between the wing surface and the mean aerodynamic chord. In the case of the STRATOFLY, that has a waverider configuration, in the denominator the total plan area of the airplane is considered instead of the wing surface, as usually occur with hypersonic aircraft that are highly integrated structures. So, the canard volume coefficient is defined as in the formula (3.1)

$$V_c = \frac{S_c l_c}{S_{ref} MAC} \tag{3.1}$$

The sizing of the surface usually starts with the selection of a reference value from the statistical population but, in this case study it is made the hypothesis that the canard volume coefficient of the MR5 is equal to the known one of MR3. Another guess taken is to consider the canard moment arm of the MR5 analogous to that of the MR3 scaled by the factor 0.68, used to scale linearly the entire configuration.

With these two starting assumptions:

- same canard volume coefficient of MR3
- $l_{c_{MR5}} = 0.68 \cdot l_{c_{MR3}}$

it is possible to write the equalities (3.2) and (3.3) with the explicit parameters.

$$V_{c_{MR5}} = V_{c_{MR3}} \tag{3.2}$$

$$\frac{S_{c_{MR3}} l_{c_{MR3}}}{S_{ref_{MR3}} MAC_{MR3}} = \frac{S_{c_{MR5}}(0.68 \cdot l_{c_{MR3}})}{S_{ref_{MR5}} MAC_{MR5}} \tag{3.3}$$

All data of the MR3 are known, the only unknown is the total plan area of the new canard, that turns out to be 66.8 m^2 after solving the equation. Subsequently, for the geometrical definition of this surface, the parameters shown in the table 3.4 are selected taking into account the respective values related to the canard of the MR3 and of other similar aircraft.

Table 3.4: Geometric parameters of MR5 Canard

Parameter	Value	Unit of measure
Total plan area of canard (S_c)	66.8	$[m^2]$
Sweep angle (Λ_c)	40	[deg]
Taper ratio (λ_c)	0.32	-
Aspect ratio (AR_c)	3.2	-

Known the canard surface and these geometric parameters, it is now possible to calculate the span, the root and tip chords with the equations (3.4), (3.5) and (3.6).

$$b_c = \sqrt{S_c AR_c} = 14.6m \tag{3.4}$$

$$c_{r_c} = \frac{2S_c}{b_c(1+\lambda_c)} = 6.93m \tag{3.5}$$

$$c_{t_c} = c_{r_c}\lambda_c = 2.21m \tag{3.6}$$

The plan drawing of the canard's surface, obtained with the procedure just seen, is reported in figure 3.2.

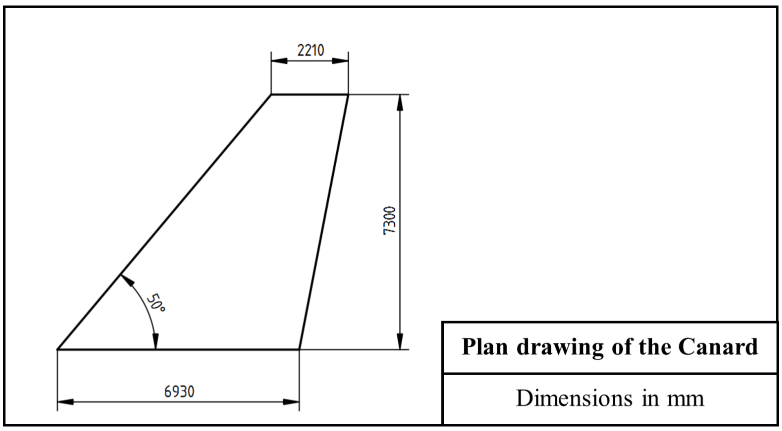

Figure 3.2: Canard

3.3 V-tail

The V-tail [9] has two sections placed to form a shape similar to the letter V, that act as both a horizontal and vertical tail. An important advantage should be the possibility to reduce the total wetted area as compared to the two separate horizontal and vertical surfaces, even if today there are some disagreements about this aspect. The forces generated on the V-tail surfaces have a component in both y and z directions, therefore they affect longitudinal and lateral-directional trim and stability. The respective mobile parts can act as both rudders and elevators, and for this reason they are usually called ruddervators. This combination of commands makes the control system of these surfaces more complex, but at the same time the reconfiguration of the system results to be easier if a failure occurs because there is already a combination of effects.

For the sizing of these surfaces, the same steps seen for the canard are followed, and the same hypothesis related to the V-tail volume coefficient and moment arm are made, that are:

- same V-tail volume coefficient of MR3
- $l_{V-tail_{MR5}} = 0.68 \cdot l_{V-tail_{MR3}}$

The equation equal to the (3.3) with the parameters of the V-tail is applied, and the only unknown that is the total plan area of both the sections is made explicit, so it is obtained the expression (3.7).

$$S_{tV_{MR5}} = \frac{S_{ref_{MR5}} MAC_{MR5} S_{tV_{MR3}}}{0.68 S_{ref_{MR3}} MAC_{MR3}} = 88.2m^2 \tag{3.7}$$

It is now possible to proceed with the geometric definition of the single surface. As seen also in the previous subsection, the following parameters are defined: sweep angle, taper ratio, aspect ratio and dihedral angle that is analogous to that of the MR3. Then, the equations (3.4), (3.5) and (3.6) are applied using these new values, to calculate the root chord, the tip chord, and the span of the single surface of the V-tail. In table 3.5, all these new data are reported.

Table 3.5: Geometric parameters of MR5 V-tail (single surface)

Parameter	**Value**	**Unit of measure**
V-tail single surface (S_V)	44.1	[m^2]
Sweep angle (Λ_V)	45	[deg]
Dihedral angle (Γ_V)	33	[deg]
Taper ratio (λ_V)	0.34	-
Aspect ratio (AR_V)	1.3	-
Root chord (c_{r_V})	8.69	[m]
Tip chord (c_{t_V})	2.95	[m]
Span (b_V)	7.57	[m]

Once sized the two sections of the V-tail, the respective mobile parts that are the rudders or ruddervators can be defined. It has been decided to calculate the area of these control surfaces using a parameter defined as the ratio between the area of the mobile part and the total surface of the V-tail. In addiction it is assumed that this ratio is equal to the respective value of the MR3, which is considered as reference and reported in (3.8).

$$\frac{S_{t_{rud_{MR3}}}}{S_{tV_{MR3}}} = 0.302 \tag{3.8}$$

Known this ratio and the total area of the V-tail, the rudders' surface can be calculated with the reverse formula, and it results to be $26.64m^2$. The next steps consist in selecting a value of the taper ratio and of the total height H of the rudder, shown in table 3.6, and in determining the major and minor chords with the equations (3.9) and (3.10).

Table 3.6: Geometric parameters of MR5 rudder (single surface)

Parameter	**Value**	**Unit of measure**
Rudder single surface (S_{rud})	13.32	$[m^2]$
Taper ratio (λ_{rud})	0.7	-
Height (H_{rud})	1.3	[m]

$$c_{M_{rud}} = \frac{2S_{rud}}{H(1+\lambda_{rud})} = 2.61m \tag{3.9}$$

$$c_{m_{rud}} = c_{M_{rud}}\lambda_{rud} = 1.83m \tag{3.10}$$

In figure 3.3 the drawing of the V-tail single surface with rudder is reported.

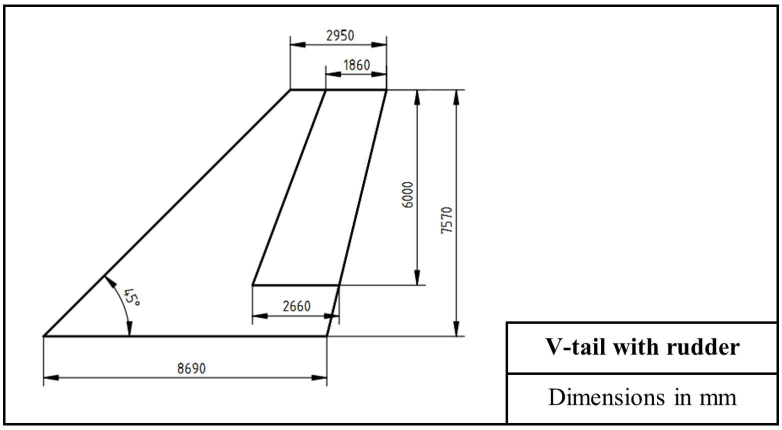

Figure 3.3: V-tail single surface with rudder

3.4 Elevon

The elevons are multi-functional surfaces positioned at the rear of the wing. They act as elevators for pitch control when there is a symmetric deflection, and as ailerons for roll control with an asymmetric deflection. On the MR5 aircraft four equal elevons, two internal and two external, are considered as on the MR3. For the sizing of these surfaces the same procedure seen for the rudder is used, but in this case the key parameter that permits to calculate the area of the elevons is defined as the ratio between the area of the mobile parts of the wing and the total plan area of the aircraft. It is assumed that this parameter of the MR5 is equal to the respective value of the MR3 that is reported in (3.11).

$$\frac{S_{t_{elevon_{MR3}}}}{S_{ref_{MR3}}} = \frac{4 \cdot 15}{2491} = 0.024 \tag{3.11}$$

Known the reference value of the surface ratio and the total plan area of the MR5, the total plan area of the elevons can be calculated with the reverse formula, and it results to be 40.7 m^2, so the single surface is equal to about 10.2 m^2.

Then a rectangular plan area of the elevon is assumed and it is supposed to have the same span of the respective mobile surfaces of the MR3, since the total wingspan has not been changed. With these two assumptions, it is possible to easily determine the constant chord of the elevon that is 2.04 m.

3.5 Body flap

The body-flaps are mobile surfaces used for the longitudinal trim and control, located on the body of the aircraft and not on the wing. Two surfaces positioned on the top of the integrated nozzle are considered for the MR5 case study, similarly to the MR3. The sizing is made following the same method used for the elevons; therefore, it is exploited the parameter (3.12) defined as the ratio between the area of these mobile surfaces and the total plan area of the aircraft, and it is considered as reference value that of the MR3.

$$\frac{S_{t_{bf_{MR3}}}}{S_{ref_{MR3}}} = \frac{2 \cdot 23.7}{2491} = 0.019 \tag{3.12}$$

Known this parameter, it is possible to calculate the area of the body-flap surfaces with the reverse formula and it results equal to 32.22 m^2. Then it is assumed that the plan surface is trapezoidal and that the major and minor spans are the same of that of the MR3, which are respectively equal to 4.05 m and 2.58 m. Finally, the axial length of the surface is calculated with the equation (3.13).

$$\frac{2 \cdot S_{bf_{MR5}}}{b_{M_{bf}} + b_{m_{bf}}} = 4.86 \quad m \tag{3.13}$$

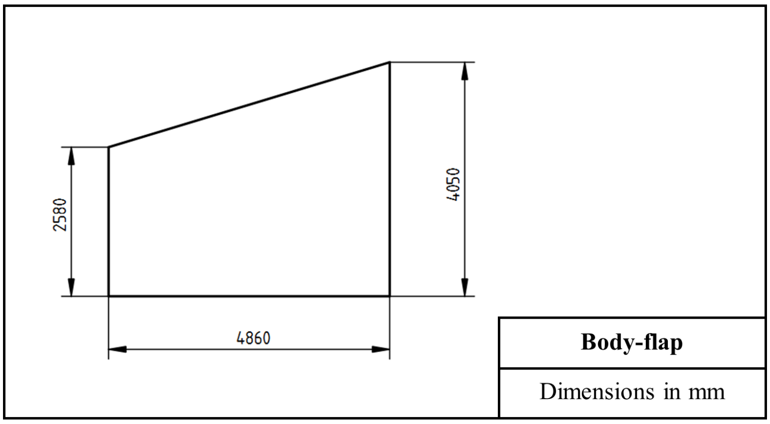

Figure 3.4: Body-flap surface

In figure 3.4 the drawing of the single body-flap surface with the new dimensions obtained is shown.

3.6 Final results

The data obtained in this chapter of all control surfaces are summarized in table 3.7, and they refer to each single surface.

Table 3.7: Control surfaces of STRATOFLY MR5

External Elevon (single surface)	
Chord [m]	2.04
Span [m]	5
Surface [m^2]	10.2
Internal Elevon (single surface)	
Chord [m]	2.04
Span [m]	5
Surface [m^2]	10.2
Canard (single surface)	
Root chord [m]	6.93
Tip chord [m]	2.21
Span [m]	7.3
Sweep angle [°]	40
Surface [m^2]	33.4
Rudder (single surface)	
Major chord [m]	2.66
Minor chord [m]	1.86
Height [m]	6
Inclination [°]	33
Surface [m^2]	13.57
Body flap (single surface)	
Major span [m]	4.05
Minor span [m]	2.58
Length [m]	4.86
Surface [m^2]	16.11

Chapter 4

Aerodynamic characterization

In this preliminary phase of the MR5 project, few starting data are available and the aerodynamic characteristics of the aircraft are not known, but it is important to have an idea of these aspects to proceed in the design, even if preliminary, of the flight control system, especially in the case of high-speed aircraft. Indeed, if the aerodynamic characterization is available, it is possible to determinate the trim in some flight conditions and so have an idea of the control surfaces deflections needed in different phases of the mission profile. The estimation of these deflections is just the next step of the design approach indicated in 1.1, after the definition of control surfaces. Finally, the hinge moment and the actuation power can be calculated knowing the deflections and it is possible to continue the definition of the FCS architecture.

An accurate aerodynamic characterization could be obtained for example by a CFD (Computational Fluid Dynamic) simulation, but in these first stages of the design there are not the necessary tools, such as the complete CAD model of the aircraft, to carry out such high-level analyses. This method has been used instead for the STRATOFLY MR3 [7]-[8], of which accurate aerodynamic databases are available. The approach used for this aircraft includes, as first step, the analysis of the clean configuration that consists of the external vehicle layout, including empennages and undeflected control surfaces, then the aerodynamic database is completed adding the contributions to lift, drag and moment coefficients of all control surfaces, whose effects are analyzed individually [7].

It has been decided to follow the same line of thought also for the MR5 concept of vehicle. Firstly, the aerodynamic characteristics of the clean configuration are evaluated using a simplified model proposed in the reference [10], then possible contributions of the control surfaces are added taking into account the available databases of the MR3, which is the reference aircraft par excellence in this project.

4.1 Simplified model

In the reference [10] three simplified aerodynamic models, found in literature, are analysed and applied to the STRATOFLY MR3. Then, the results obtained are compared with the aerodynamic data available, and from this comparison the model that better predicts the aerodynamic characteristics of the aircraft seems to be the All-body hypersonic one.

Furthermore, in the second part of the reference, some corrections are introduced in the model to reduce the gap between the results and the correct data. In addition to the use of a simplified aerodynamic model, this gap is due also to the fact that the method refers to an aircraft configuration different from the STRATOFLY MR3 and MR5 waverider one. Therefore, it has been decided to use this model with the corrections suggested by the reference [10] for the preliminary estimation of the aerodynamic coefficients of the MR5 clean configuration.

The starting model is presented in the reference [11] and it aims to estimate the aerodynamic performance of a representative family of all-body hypersonic aircraft. Their configuration is characterized by a delta planform with an elliptical cone forebody and an elliptical cross-section afterbody. The body shape is defined by the following three independent parameters:

- sweep angle of the body leading edge (Λ)
- breakpoint length ratio (l_π/l), which specify the position of the breakpoint between the forebody and afterbody,
- fatness ratio specified as the ratio of the maximum cross-section area to the total planform area (S_π/S).

An example of the configuration described above is reported in figure 4.1, where there are also indicated the characteristic parameters.

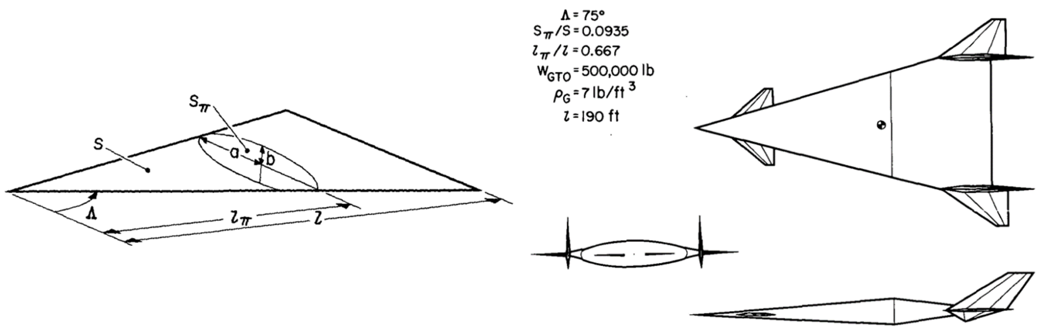

Figure 4.1: All-body hypersonic aircraft configuration

The lift and drag coefficients of the MR5 are estimated applying some non-linear relations reported in detail in the appendix A. These equations are very similar to those used in the reference [11] but they have the corrections taken from the reference [10].

4.2 Lift coefficient

The lift coefficient (C_L) of the clean configuration is estimated with the equation (4.1), where it is possible to note the explicit dependence on the angle of attack. Furthermore, in the relation there are two coefficients C_1 and C_2 that depend on Mach number and aspect ratio of the aircraft; for detailed information on the expressions used to estimate these, see the appendix A. Finally, the equation also includes the parameter C_{L_0} that is the value of the lift coefficient when the angle of attack is zero. One of the corrections suggested by the reference [10] consists precisely in the addition of this parameter, which translates the lift coefficient curves and cannot be estimated by the starting model. Unfortunately, this value is not known for the STRATOFLY MR5, for which it is considered the same value of the MR3, whose aerodynamic databases are all available.

$$C_L = C_{L_0} + C_1 sin(\alpha) + C_2 sin^2(\alpha) \tag{4.1}$$

The lift coefficient curves obtained as function of the angle of attack are shown in the figures 4.2, 4.3 and 4.4, which refer to different Mach number.

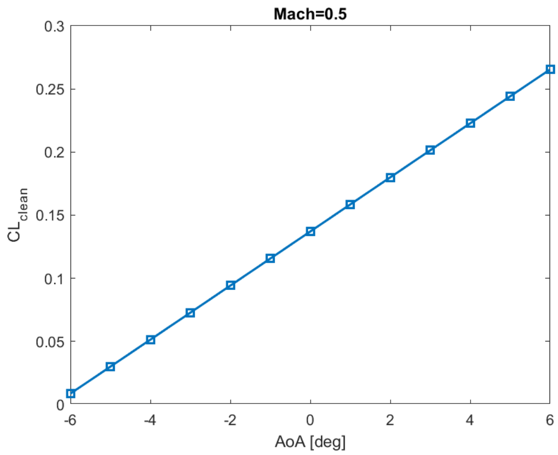

Figure 4.2: $C_{L_{clean}}$ versus AoA at M=0.5

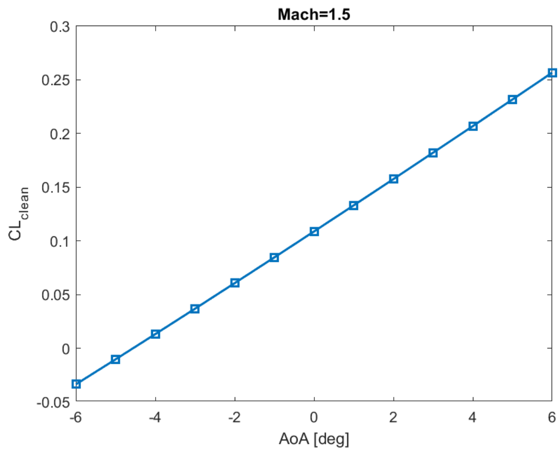

Figure 4.3: $C_{L_{clean}}$ versus AoA at M=1.5

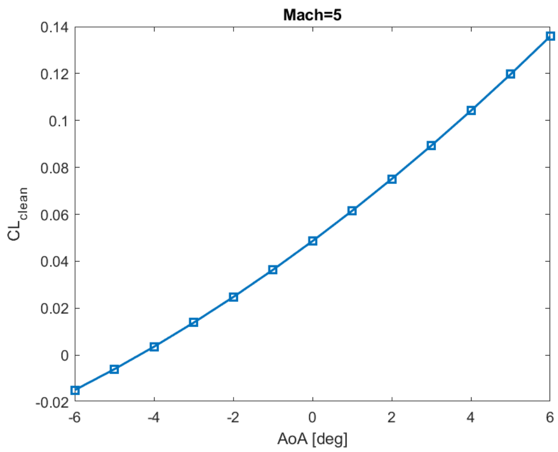

Figure 4.4: $C_{L_{clean}}$ versus AoA at M=5

In figure 4.5, the trends related to different Mach numbers are reported in the same graph, and it is possible to note that the aerodynamic coefficient always increases as the angle of attack rises but with different slope according to the flight regime. In the subsonic regime the increase in the Mach number leads to an increase in the slope, therefore with the same increment of the angle of attack, there is a greater increase in the lift coefficient at higher Mach. While in supersonic regime the curves are translated lower, so with the same angle of attack there are smaller values of lift coefficients than in the subsonic cases, furthermore the curves' slope decreases as the velocity increases, therefore with the same variations of the angle of attack, there are slighter changes of the lift coefficient as Mach number increases.

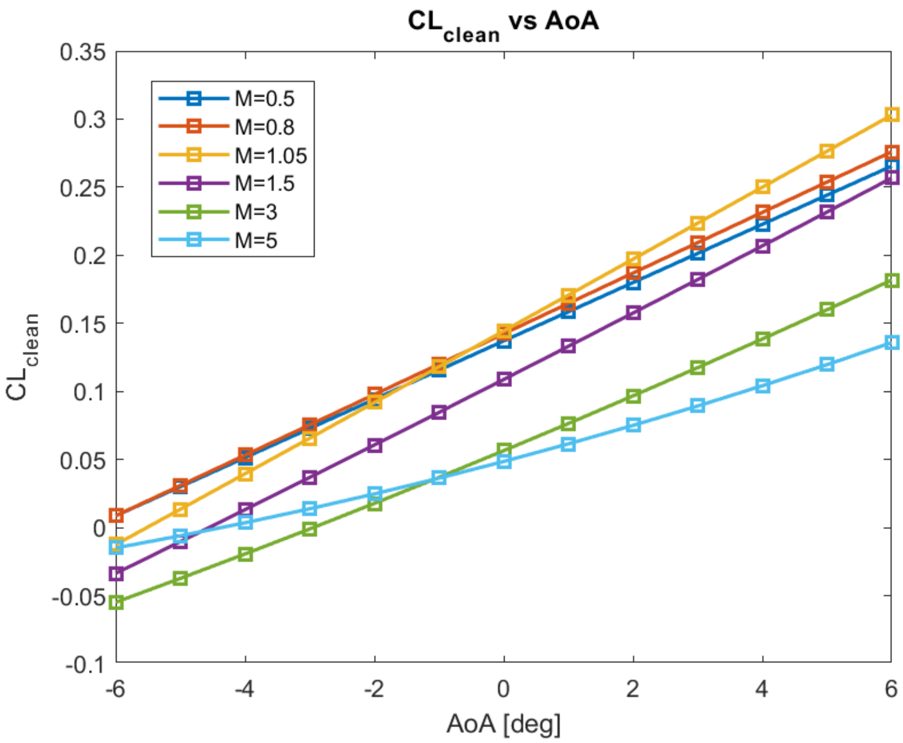

Figure 4.5: $C_{L_{clean}}$ versus AoA

Finally, the lift coefficient trends as function of the Mach number at a given angle of attack are shown in figures 4.6 and 4.7. In particular, in figure 4.6 the zero angle of attack is considered, therefore the curve corresponds to C_{L_0} whose values are the same of the STRATOFLY MR3, while the figure 4.7 is related to the angle of attack equal to -1°. As already seen in the previous images, it can be noted a change in behavior going from low to high speed; with the same angle of attack as Mach number increases, the lift coefficient increases in the subsonic regime and decreases in the supersonic one.

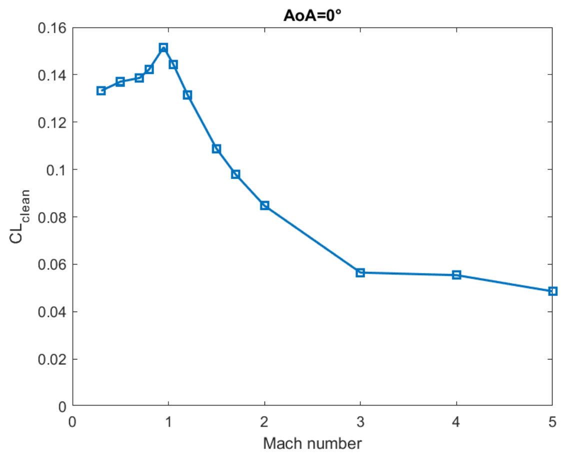

Figure 4.6: $C_{L_{clean}}$ vs Mach at AoA=0°

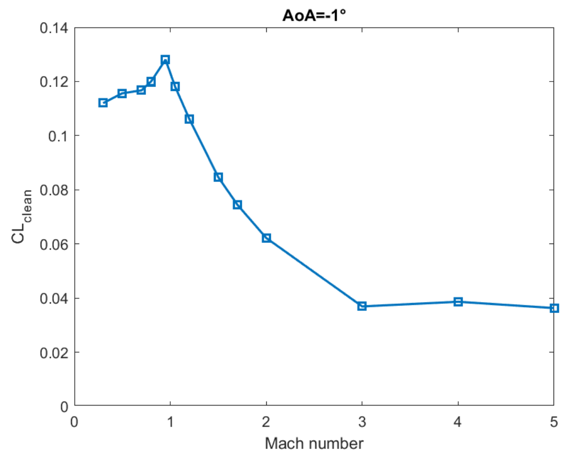

Figure 4.7: $C_{L_{clean}}$ vs Mach at AoA=-1°

4.3 Drag coefficient

The clean drag coefficient is obtained using the equation (4.2), where there is the sum of three contributions: the induced drag, the zero-lift body drag and the zero-lift V-tail drag. The relations used to calculate each of these coefficients are shown in the appendix A.

$$C_D = C_{D_0} + C_{D_{0VT}} + C_{D_i} \tag{4.2}$$

- **Induced drag** (C_{D_i})

  The induced drag coefficient depends on both angle of attack and Mach number. In the reference [11] for the estimation of this contribution there are some equations for the sharp leading edge delta wing modified by a coefficient to account for the rounded leading edge of the elliptic cone, which characterized the reference configuration of the all-body hypersonic model. However, the mathematical expressions used in this case study and also shown in the appendix are those of the reference [10] that have some corrections introduced to better estimate the curves' slope of the MR3, therefore it is hoped that they will be able to better predict also the trend of the drag coefficient of the MR5, whose configuration is more similar to that of the STRATOFLY MR3.

- **Zero-lift body drag** (C_{D_0})

  The zero-lift body drag coefficient is obtained by the sum of three contributions: body pressure drag, body friction drag and body bluntness drag, as indicated in the relation (4.3).

  $$C_{D_0} = C_{D_{PB}} + C_{D_{FB}} + C_{D_{BB}} \tag{4.3}$$

  In the subsonic regime the pressure drag coefficient is assumed to be zero because generally its values are small, in transonic regime it is supposed to vary linearly with respect to Mach number, while in supersonic conditions this contribution is calculated integrating the pressure distribution on the body of the aircraft [11].

The body friction drag coefficient is determined with the relation used in the reference [10] for the STRATOFLY MR3, this is not taken from the simplified starting model, and it is also reported in the appendix.

Finally, the body bluntness drag contribution is considered zero in the subsonic regime, it is assumed to vary linearly with respect to Mach number in the transonic conditions, and in the supersonic regime it is calculated using a Newtonian flow approximation [11].

- **Zero-lift V-tail drag** ($C_{D_{0VT}}$)

  This coefficient allows to consider the drag contribution given by the V-tail's surfaces, and it is defined as the zero-lift body drag by the sum of pressure, friction and leading-edge bluntness components. The equations used are reported in detail in the appendix A. The addition of this contribution is necessary to estimate the drag of the complete clean configuration that consists of the external vehicle layout, including V-tail and undeflected control surfaces.

  It can be noted that the drag contribution given by the canard is not considered in this phase because in the treatment of the aerodynamic characterization of the STRATOFLY MR3 [8] the clean configuration does not include this surface that is added in a second moment, therefore also for this concept of vehicle it has been decided to not consider the canard in the drag coefficient determination of the clean configuration. The effect on lift and drag coefficient of the canard, as that of the other control surfaces will be added later.

The drag coefficient curves as function of the Mach number at angle of attack equal to -1° and 0° are shown in the figure 4.8 and 4.9. The blue trends are obtained considering all the contributions of drag coefficient previously seen and calculated with the equations written in the appendix A.

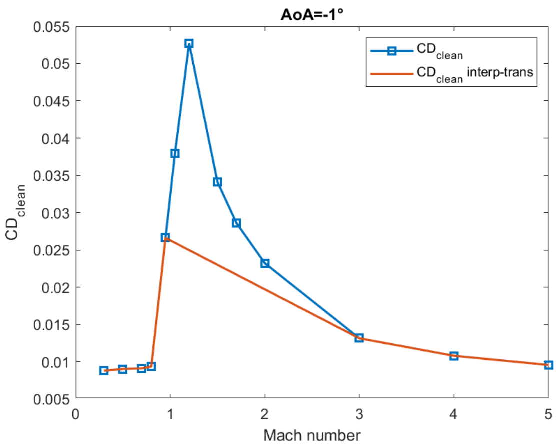

Figure 4.8: $C_{D_{clean}}$ vs Mach at AoA=-1°

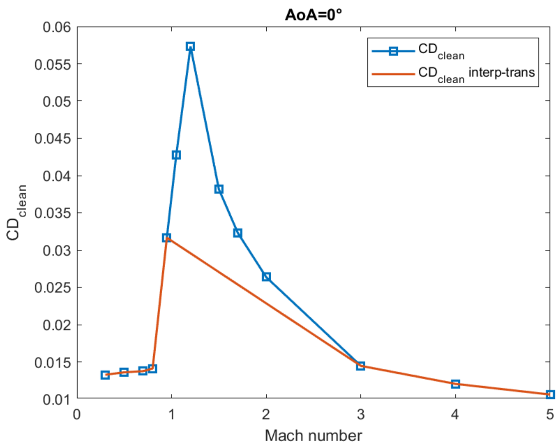

Figure 4.9: $C_{D_{clean}}$ vs Mach at AoA=0°

It can be noted that the highest drag values are recorded in the transonic regime, this behavior is generally correct because around M=1 the shock waves begin to arise and they lead to the birth of the wave drag contribution, then as Mach number increases in supersonic regime the overall drag decreases. However, in the reference [10] it is noted that the data obtained in the transonic regime with the simplified model are inaccurate results because too high; therefore, it is proposed a correction that consists in considering a linear interpolation with respect to Mach number from M=1 to M=3, and this leads to the red curve shown in the figure 4.8 and 4.9.

Finally, the clean drag coefficient corrected as function of the angle of attack for different Mach numbers is reported in figure 4.10. It can be observed that the curves translated above, so with the highest drag values are those associated with the transonic speeds, M=1.05 and M=1.5, as already seen in the previous graphs.

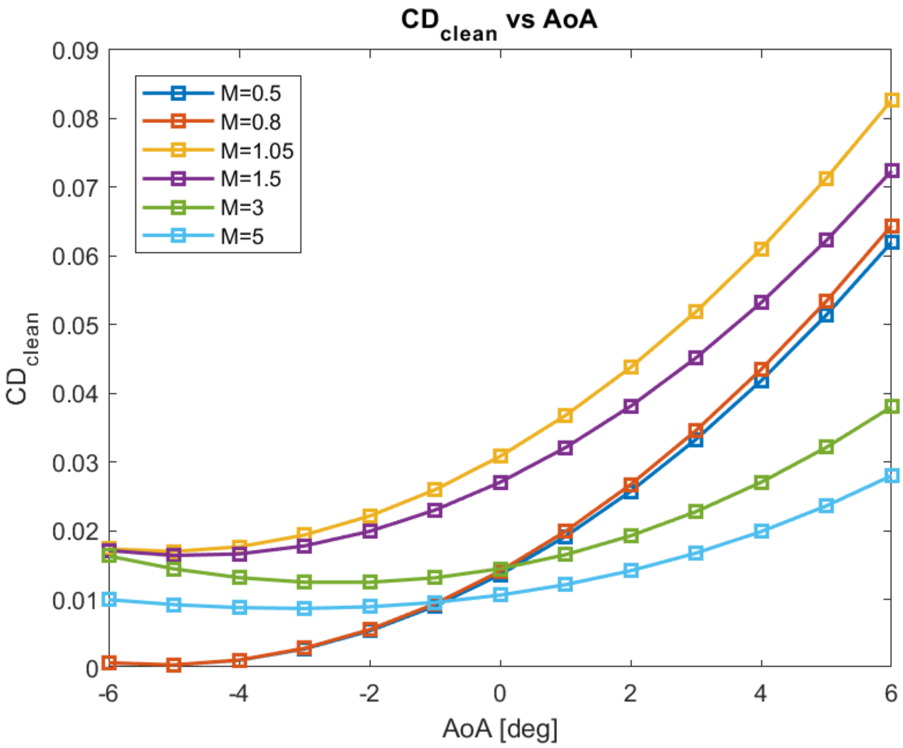

Figure 4.10: $C_{D_{clean}}$ versus AoA

4.4 Effect of control surfaces

As already mentioned at the beginning of this chapter, the simplified aerodynamic model was applied only to the clean configuration that includes the entire aircraft with the undeflected control surfaces and without the canard. However, the data obtained are incomplete because the deflection of any control surface causes a change in the forces acting on the aircraft, and therefore a displacement of the lift and drag curves seen in the previous sections. The overall lift and drag can be calculated adding the contribution due to the deflection of each control surface to the values of the clean configuration as indicated in the equations (4.4) and (4.5).

$$C_L = C_{L_{clean}} + \sum_{i=1}^{n} (\Delta C_L)_i \tag{4.4}$$

$$C_D = C_{D_{clean}} + \sum_{i=1}^{n} (\Delta C_D)_i \tag{4.5}$$

This type of approach has been applied also to the aerodynamic characterization of the STRATOFLY MR3. The effect of control surfaces has been estimated through inviscid CFD simulations that have allowed to create an aerodynamic database with all the contributions ΔC_{j_i} related to each control surface and respective deflection as Mach number and angle of attack vary. At this stage of the design, analyzes of this kind cannot be done for the MR5 concept of vehicle but its control surfaces and configuration are very similar to that of the MR3, even if the dimensions and proportions are different; for these reasons it has been decided to use the complete database of the STRATOFLY MR3 to have at least an idea of what the effect of control surfaces might be on the aerodynamic characteristics of the MR5. For the estimation of these contributions the relations (4.6) and (4.7) are considered.

$$[(\Delta C_L)_i]_{MR5} = \frac{[(\Delta C_L)_i]_{MR3}}{[C_{L_{clean}}]_{MR3}} \cdot [C_{L_{clean}}]_{MR5} \tag{4.6}$$

$$[(\Delta C_D)_i]_{MR5} = \frac{[(\Delta C_D)_i]_{MR3}}{[C_{D_{clean}}]_{MR3}} \cdot [C_{D_{clean}}]_{MR5} \tag{4.7}$$

It is noted that the data obtained in this chapter for the MR5 cannot be considered particularly correct because they are due to the application of a simplified aerodynamic model as regards the clean configuration and due to these last simplified relations that are supposed as regards the contributions of the control surfaces; however, in this preliminary phase with not much available data the database obtained can be a good starting point to have an idea of the aerodynamic performances of the aircraft and to proceed in the preliminary design of the flight control system.

Chapter 5

Longitudinal static stability analysis

5.1 Aerodynamic static stability

The longitudinal static stability is an important aspect that consists in the tendency of the aircraft to return in its starting trim condition after an external perturbation occurs. The plane might be intrinsically stable or not, and in some cases even if it is stable, it might not meet the stability requirements imposed; in these last situations it is necessary to introduce accurate active control system that allow to overcome these limits. The high-speed vehicles very often have stability problems mainly because in their mission profile they go through very different flight regimes that lead to a variation of the aerodynamic behavior of the configuration and generally to the shift of the aerodynamic center. The longitudinal static stability condition is reported in the relation (5.1), and it consists in having a negative derivative of the pitching moment coefficient with respect to the angle of attack.

$$\frac{\delta C_{M_y}}{\delta \alpha} < 0 \tag{5.1}$$

In this case study the pitching moment coefficient with respect to the center of gravity can be calculated using the lift and drag coefficients estimated in the previous chapter. These values are the components of the aerodynamic forces acting on the aircraft respectively in the direction perpendicular and parallel to the velocity vector (see figure 5.1). Knowing these coefficients, the respective components in the body axes can be calculated with the equations (5.2), and then the pitching moment coefficient with respect to the center of gravity can be estimated using the relation (5.3) where $x_{SM} = (x_{GC} - x_{ac})$ is the static margin.

$$\begin{cases} C_x = C_D cos(\alpha) - C_L sin(\alpha) \\ C_z = C_L cos(\alpha) + C_D sin(\alpha) \end{cases} \tag{5.2}$$

$$C_{M_y} = C_z \frac{x_{GC} - x_{ac}}{MAC} \tag{5.3}$$

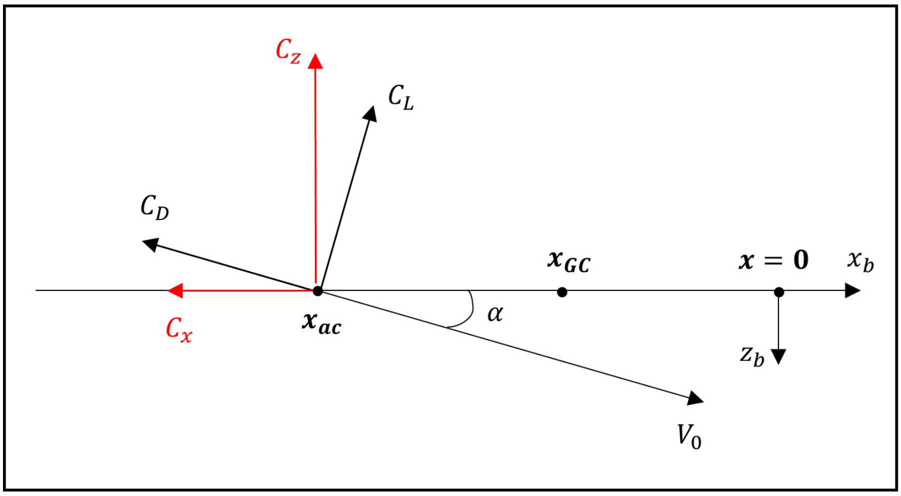

Figure 5.1: Forces in body axes

It is noted that the application of the equation (5.3) needs the knowledge of center of gravity and aerodynamic center positions, which are not estimated for the STRATOFLY MR5. For this reason, it has been decided to exploit the available data of the MR3 aircraft, in particular the position of the aerodynamic center in the different flight conditions is reported in the aerodynamic databases, while the center of gravity was calculated by a system engineering team that considered a different value for each Mach number depending on fuel consumption along the flight [8]. For the MR5 it is assumed to have the same behavior of the respective characteristic points of the MR3, but it is applied the scaling factor 0.68 used at the beginning for the configuration redesign, to estimate the new axial positions of these points. As regards the center of gravity of the MR3, the variation range was from 53 m at the beginning of the mission with low Mach number, to 48 m at the cruise phase with Mach 8; therefore, it is assumed a shift of the MR5 center of gravity between 32.68 m and 36.08 m.

Considering the stability condition (5.1) it is possible to determine the partial differentiation of the pitching moment coefficient equation (5.3) with respect to the angle of attack, and thus the relation (5.4) is obtained, and it is required to be negative.

$$C_{M_{y_\alpha}} = \frac{dC_z}{d\alpha}\frac{x_{GC} - x_{ac}}{MAC} - C_z\frac{dx_{ac}}{d\alpha} < 0 \tag{5.4}$$

It can be noted that the stability condition is satisfied not only if the static margin is negative ($x_{GC} - x_{ac} < 0$), and thus if the center of gravity is further forward of the aerodynamic center, but there are also other terms to be considered, that are: $\frac{dC_z}{d\alpha}$ which results to be positive, C_z, and $\frac{dx_{ac}}{d\alpha}$ which takes into account the fact that the aerodynamic center is not fixed but it moves according to the flight conditions, the Mach number and angle of attack. In particular, the shift of the aerodynamic center obtained as indicated above and the two limit positions of center of gravity are shown in figures 5.2 and 5.3.

In figure 5.2 the shift of the aerodynamic center as Mach number varies is shown at some fixed angles of attack, while in figure 5.3 the variation of this position as function of the angle of attack for some fixed Mach numbers is reported and, it can be noted that the

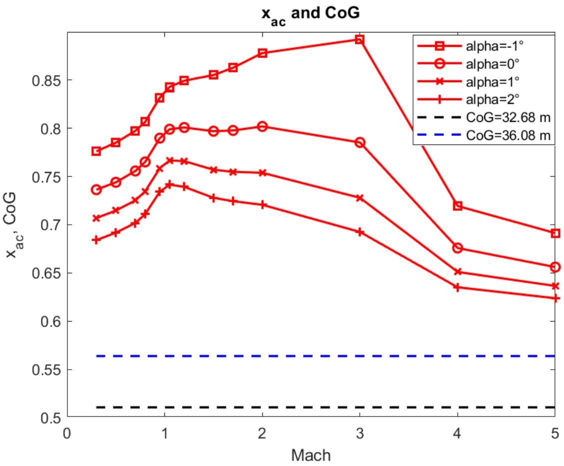

Figure 5.2: x_{ac} and CoG vs Mach number

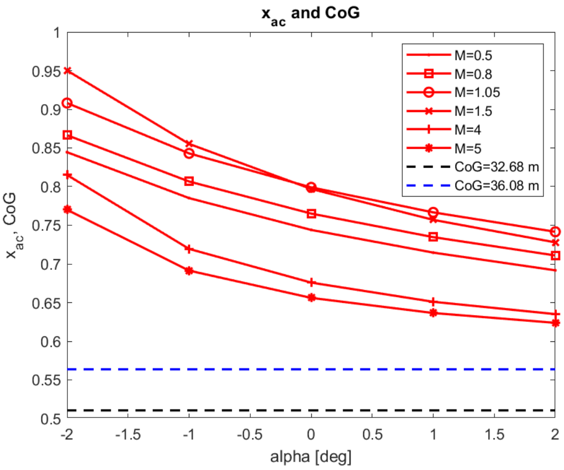

Figure 5.3: x_{ac} and CoG vs AoA

trend of this curves is always decreasing, thus the terms $\frac{dx_{ac}}{d\alpha}$ is less than zero. Furthermore it can be observed that the aerodynamic center is further back from the center of gravity for each angle of attack and Mach number, thus the static margin $(x_{GC} - x_{ac})$ is negative.

Finally, it is pointed out that the position of the aerodynamic center shown in figures is related to the clean configuration, and the addition of the deflections of control surfaces leads to changes in this point location.

In the following sections a preliminary analysis of stability is done on the basis of data previously obtained in the different flight regimes, in which the STRATOFLY MR5 will fly, in particular some reference flight conditions are selected differentiating between subsonic, transonic and supersonic regimes. Furthermore, the effect of control surfaces on longitudinal static stability are analized, and it is anticipated that the ranges of their deflections are assumed to be equal to those of the MR3 that are: $[-30 - 5]deg$ for body-flaps, $[-20 \quad 20]deg$ for canard and $[-20 \quad 20]deg$ for elevons.

5.2 Subsonic regime

The reference flight conditions considered in the subsonic regime are M=0.5 and M=0.8. Firstly, the trend of the pitching moment coefficient of the clean configuration is analyzed and it is shown in figure 5.4. It can be noted that there are two curves for each flight condition because the moment was calculated with respect to the two limit positions of center of gravity, in particular the continuous lines are related to M=0.5, while the discontinuous ones to M=0.8. In addition, it can be observed that the red curves which have the further back center of gravity are characterized by a positive slope, and thus in these conditions the clean configuration is intrinsically unstable, on the contrary with the center of gravity equal to 32.68 m it is stable or at least nearly stable.

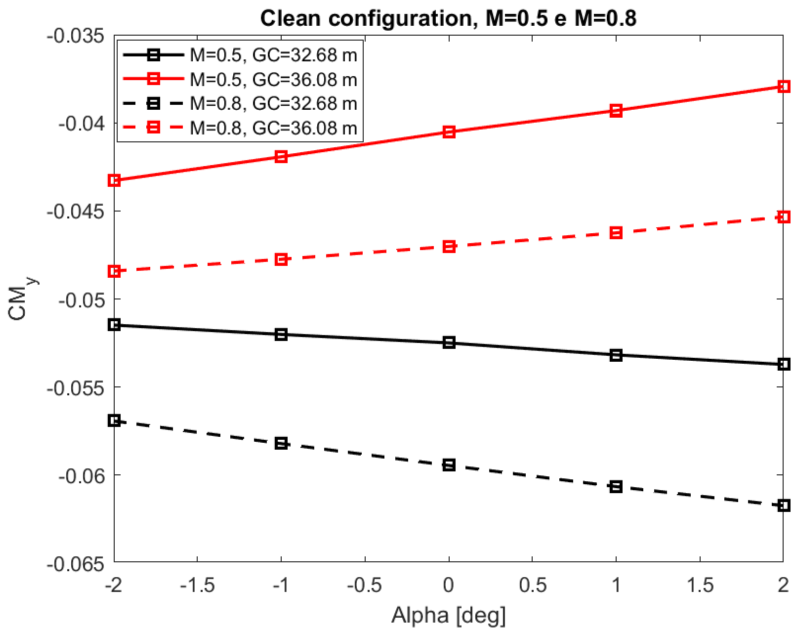

Figure 5.4: Pitching moment coefficeint vs AoA at M=0.5 and M=0.8

5.2.1 Effect of canard deflection

In this subsection it is analyzed how the curves of pitching moment coefficient change with the addition of canard and as its deflection varies. The trends as function of the angle of attack with positive and negative deflections of canard are shown in figure 5.5 and 5.6 respectively at M=0.5 and M=0.8 and related to the further forward position of center of gravity. The black lines are associated to the clean configuration, which is stable or at least nearly stable in these conditions, but it can be noted that the simple addition of canard with zero deflection destabilizes the configuration; this is mainly due to the fact that the canard is a surface positioned near the nose of the aircraft and thus it leads to a forward shift of the aerodynamic center. As the deflection of canard increases there is an attenuation of this effect, but the tendency is to destabilize the aircraft.

Furthermore, it can be observed that the positive deflections move up the curves because they cause an increment of lift near the nose forward of the center of gravity, thus the aircraft tends to pitch up and there is a positive increase in pitching moment. On the contrary with negative deflections of canard the curves move toward lower values.

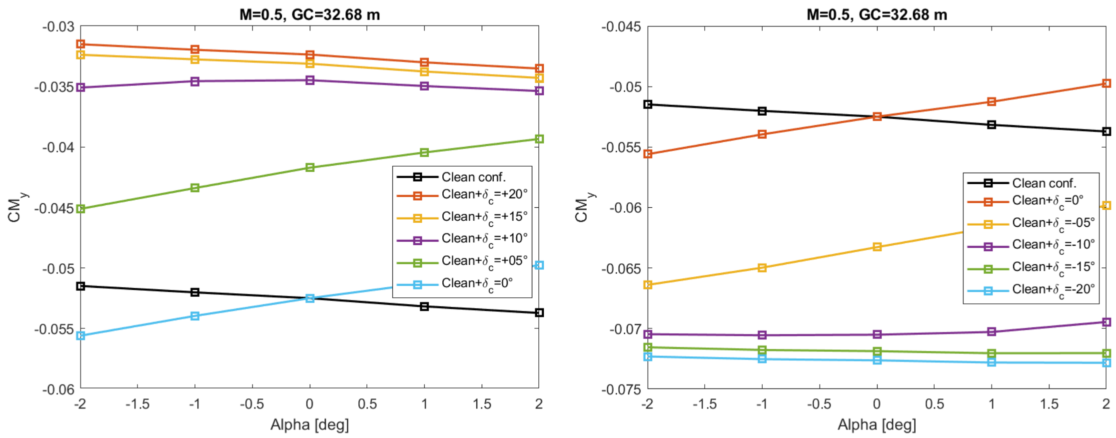

(a) *Positive Canard defections* (b) *Negative Canard deflections*

Figure 5.5: Effect of Canard at M=0.5 and CoG=32.68 m

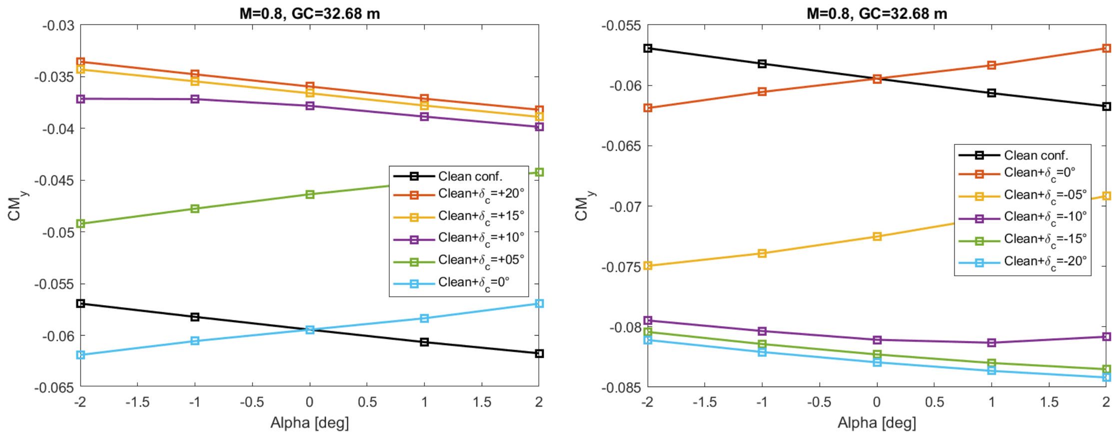

(a) *Positive Canard defections* (b) *Negative Canard deflections*

Figure 5.6: Effect of Canard at M=0.8 and CoG=32.68 m

In figures 5.7 and 5.8 are instead reported the pitching moment coefficient trends at the same conditions seen before but related to the further back limit position of center of gravity that is equal to 36.08 m. In this case the clean configuration is just unstable, and the addition of canard further destabilizes the aircraft causing an increase of the positive slope.

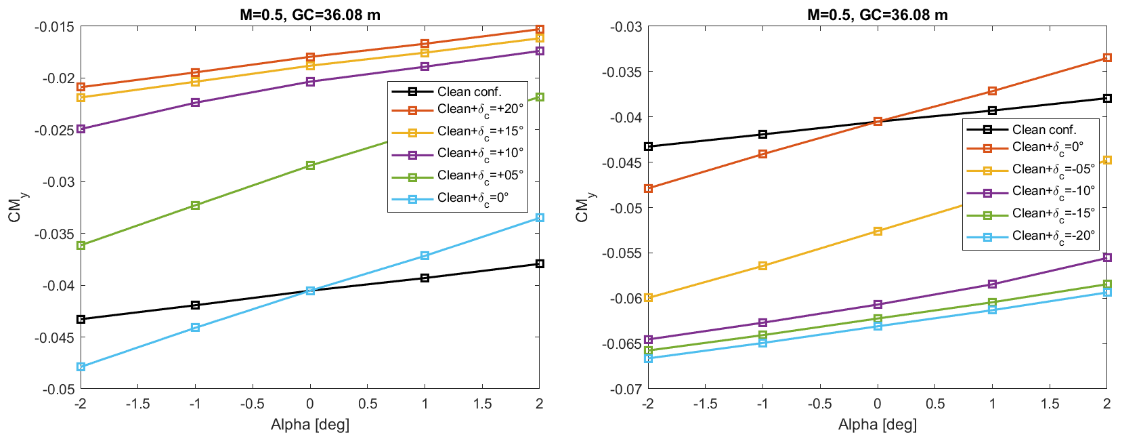

(a) *Positive Canard defections* (b) *Negative Canard deflections*

Figure 5.7: Effect of Canard at M=0.5 and CoG=36.08 m

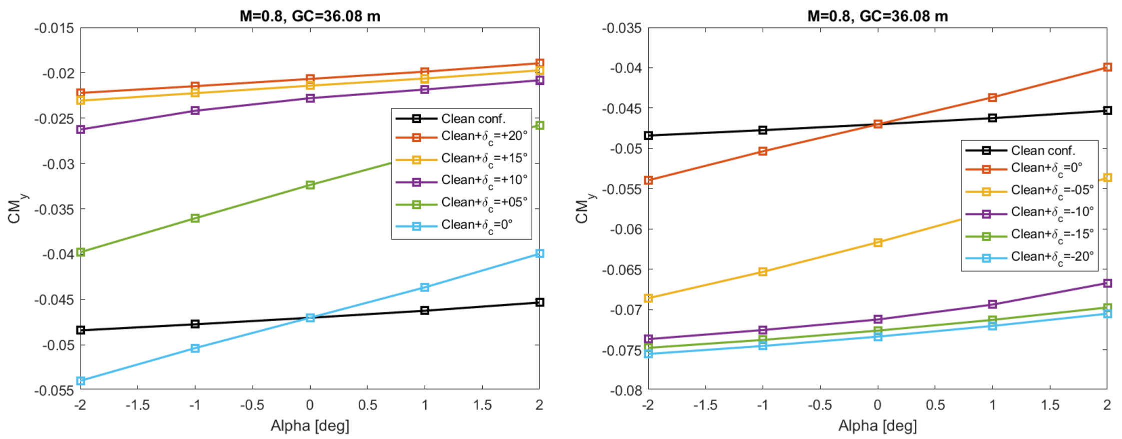

(a) *Positive Canard defections* (b) *Negative Canard deflections*

Figure 5.8: Effect of Canard at M=0.8 and CoG=36.08 m

5.2.2 Effect of elevon deflection

In this subsection the effect of elevon deflections on longitudinal static stability is analyzed. The pitching moment coefficient trends with respect to the further forward position of center of gravity and as function of the angle of attack are reported in figures 5.9 and 5.10 respectively at M=0.5 and M=0.8. Each curve is associated to different deflections of elevon, and it can be noted that they occupy different positions, but their slope is almost completely unchanged compared to the black curves that represent the clean configuration with undeflected surfaces. Therefore, the rotation of elevons leads to move the curves, and thus to a positive or negative increment in the pitching moment, useful in the determination of the trim conditions, but it does not significantly affect the stability of the aircraft.

Finally, it is observed that the figures 5.9a and 5.10a show positive deflections of elevons that move the curves toward lower values because rotating these surfaces downwards there is an increase in lift in the rear part of the wing behind the center of gravity, thus a negative contribution is added to the pitching moment that decreases, while the figures 5.9b and 5.10b show the negative deflections, which lead to an increase in negative lift at these surfaces, and thus to a positive contribution to pitching.

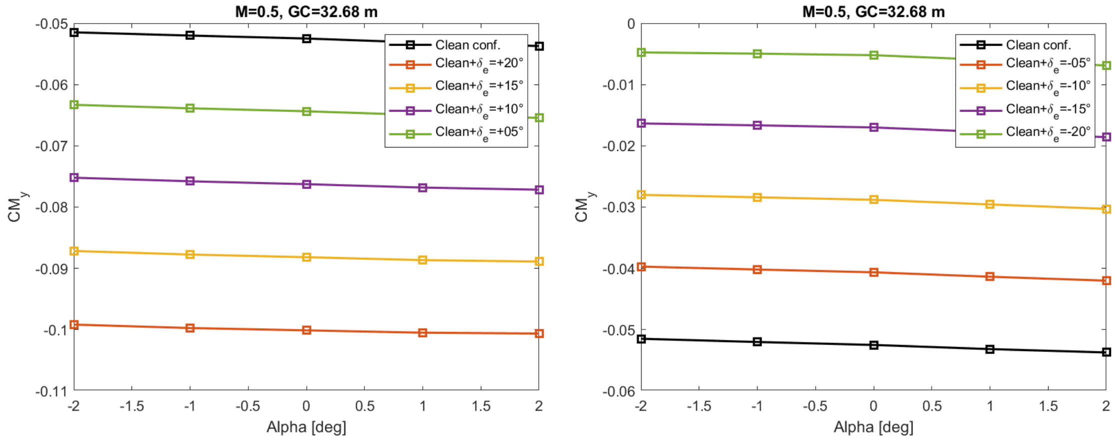

(a) *Positive Elevon defections* (b) *Negative Elevon deflections*

Figure 5.9: Effect of Elevon at M=0.5 and CoG=32.68 m

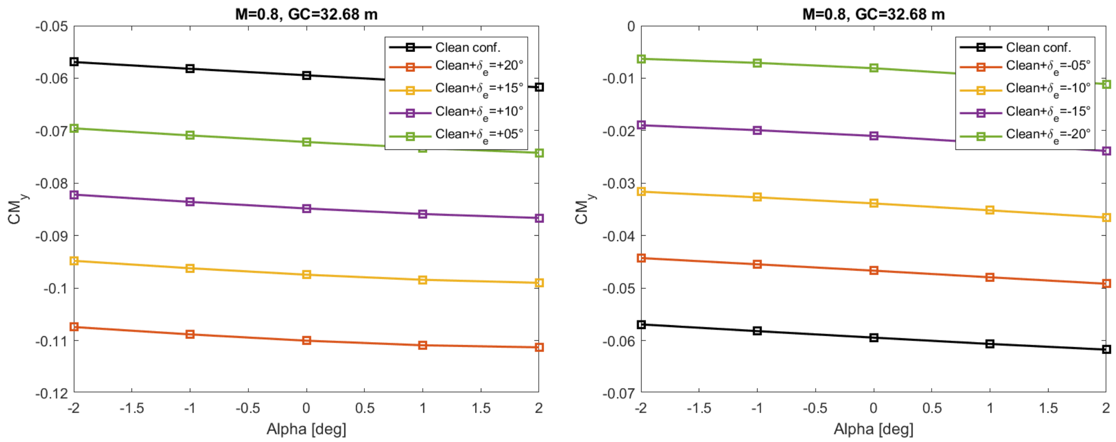

(a) *Positive Elevon defections* (b) *Negative Elevon deflections*

Figure 5.10: Effect of Elevon at M=0.8 and CoG=32.68 m

The curves similar to those just seen, but with respect to the center of gravity of 36.08 m, are reported in figures 5.11 and 5.12. The considerations previously made on the effect of elevon deflections continue to be valid, indeed the configuration that is already unstable with undeflected control surfaces remains so even if the elevons are rotated.

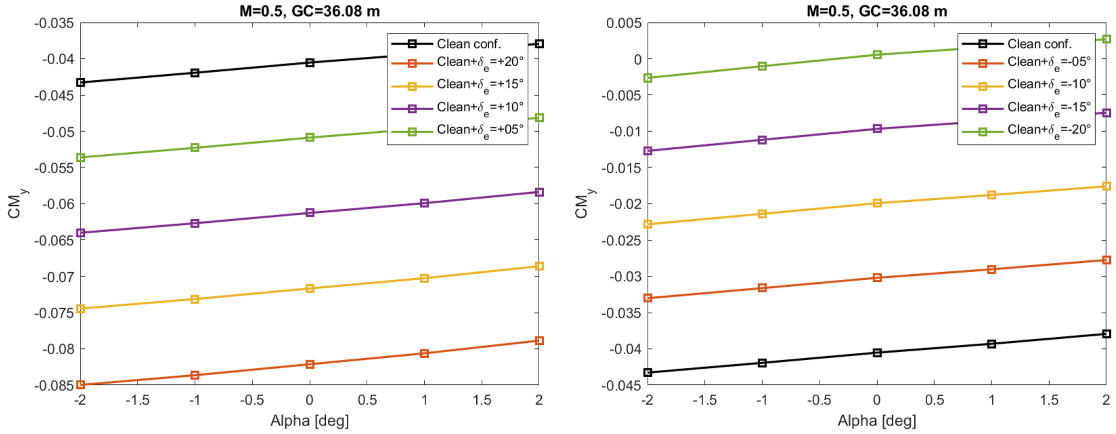

(a) *Positive Elevon defections* (b) *Negative Elevon deflections*

Figure 5.11: Effect of Elevon at M=0.5 and CoG=36.08 m

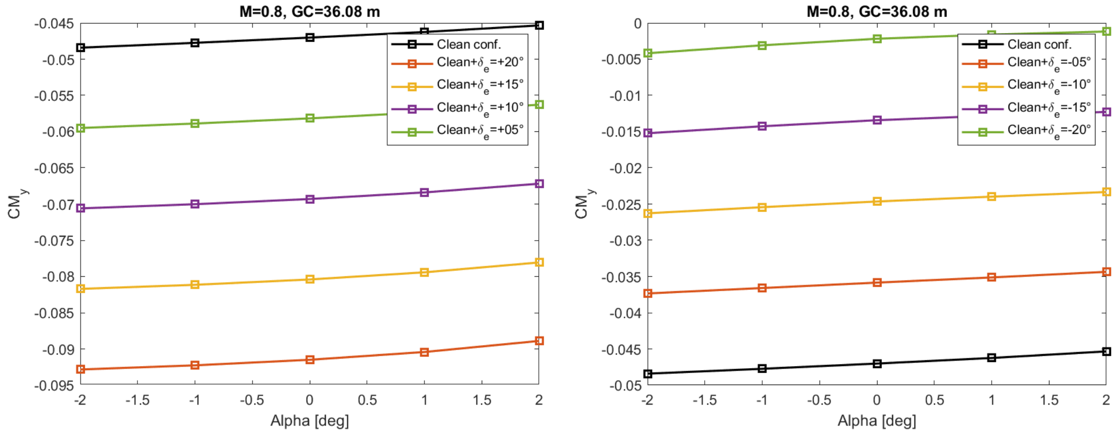

(a) *Positive Elevon defections* (b) *Negative Elevon deflections*

Figure 5.12: Effect of Elevon at M=0.8 and CoG=36.08 m

5.2.3 Effect of body-flap deflection

The last control surfaces whose effect on longitudinal static stability is analyzed are the body-flaps. These surfaces can be rotated only upwards, and these negative deflections lead to an increase in negative lift near the surfaces that are positioned in the rear part of the aircraft behind the center of gravity; therefore, they cause a positive contribution in pitching that move the respective moment coefficient curves upwards, always with respect to the black line associated to the clean configuration.

The trends with respect to the further forward position of center of gravity at M=0.5 and M=0.8 are shown in figure 5.13. It can be noted that in both cases the clean configuration is stable or nearly stable, and the deflection of body-flaps generally tends to further increase the stability of the aircraft, furthermore this positive aspect improves as the deflection increases.

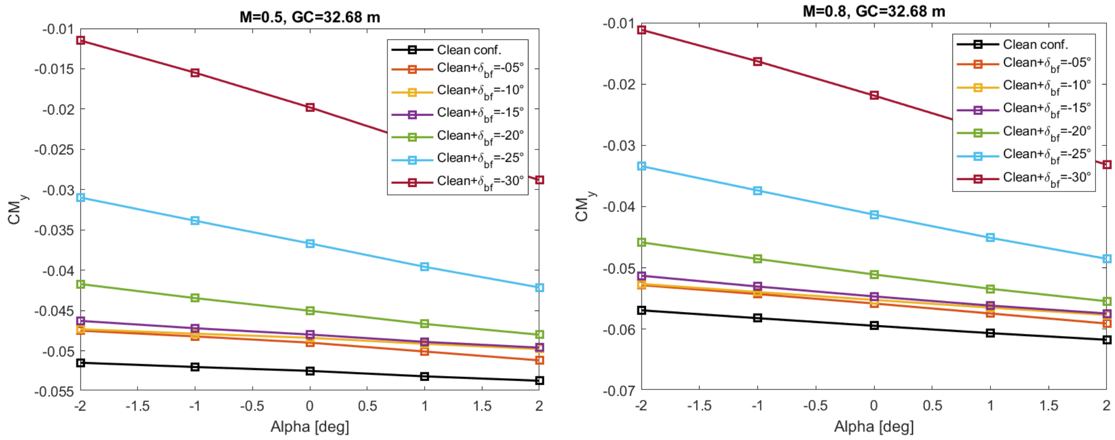

(a) *Body-flap defections at M=0.5* (b) *Body-flap deflections at M=0.8*

Figure 5.13: Effect of body-flap with CoG=32.68 m
(subsonic regime)

The curves with respect to the further back position of center of gravity are instead reported in figure 5.14. In this cases the starting clean configuration is unstable, but the deflection of body-flaps, particularly of -25° and -30°, is able to stabilize the aircraft.

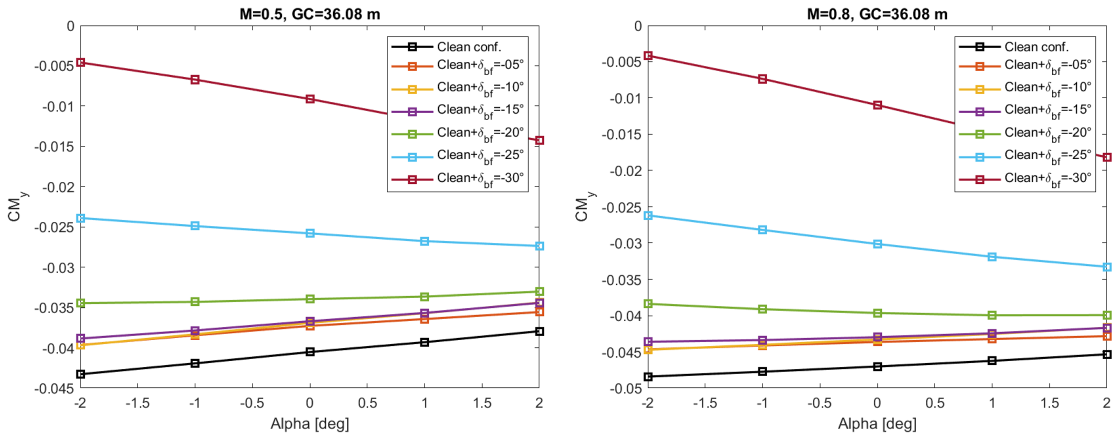

(a) *Body-flap defections at M=0.5* (b) *Body-flap deflections at M=0.8*

Figure 5.14: Effect of body-flap with CoG=36.08 m
(subsonic regime)

5.3 Transonic regime

The two reference conditions considered for the transonic regime are M=1.05 and M=1.5. The pitching moment coefficient curves related to the clean configuration in these flight conditions are reported in figure 5.15 as seen also for the subsonic regime. It is noted that the black lines associated to the further forward position of the center of gravity have a negative slope, and thus the configuration is intrinsecally stable, while the red curves related to the other limit position of center of gravity are characterized by an almost zero slope, thus the aircraft seems to be neutrally stable, and this is not acceptable. Nevertheless, at these higher values of Mach number there is an improvement from the point of view of stability compared to the results previously seen about the subsonic regime.

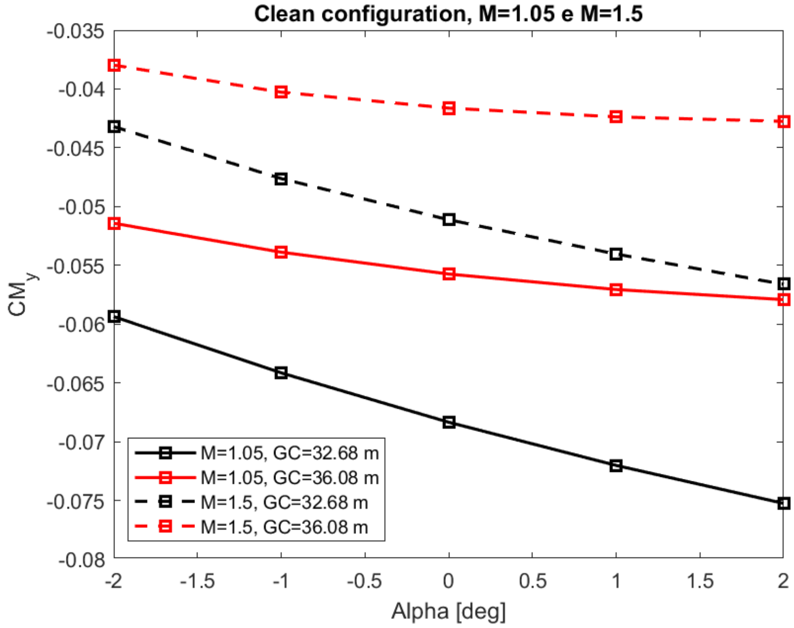

Figure 5.15: Pitching moment coefficeint vs AoA at M=1.05 and M=1.5

5.3.1 Effect of canard deflection

The addition of canard tends to destabilize the aircraft also in these new flight conditions. In figures 5.16 and 5.17 it is shown the effect of canard deflections on the pitching moment coefficient curves related to the two limit positions of the center of gravity. In particular, the figures 5.16a and 5.16b are associated to the center of gravity equal to 32.68 m and it can be noted that the configuration, which is stable with undeflected control surfaces, remains so or becames neutrally stable after the rotation of canard, while the figures 5.17a and 5.17b are related to the center of gravity equal to 36.08 m and it is shown that the clean configuration is already almost neutrally stable, thus the aircraft with deflected canard becomes unstable.

Furthermore, it should be noted that in this subsection and in the following ones, only the positive deflections of canard and elevons will be considered because the curves associated to the negative rotations are very similar but they are traslated to the opposite side of the black lines related to the clean configuration (see as examples complete graphs in section 5.2).

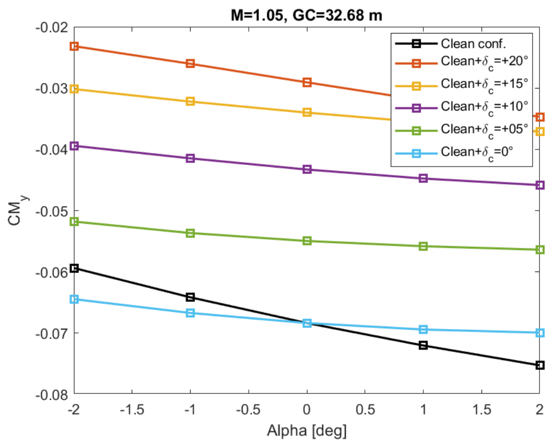

(a) *Canard defections at M=1.05*

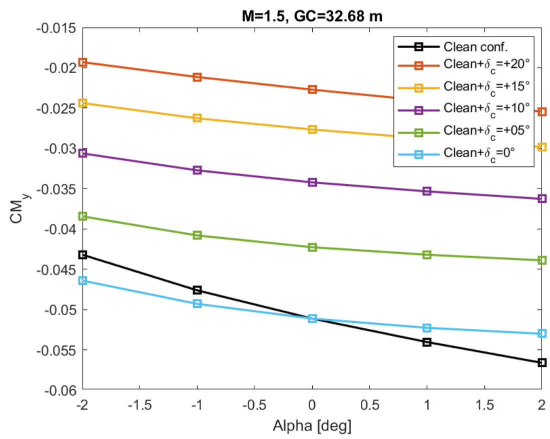

(b) *Canard deflections at M=1.5*

Figure 5.16: Effect of canard with CoG=32.68 m
(transonic regime)

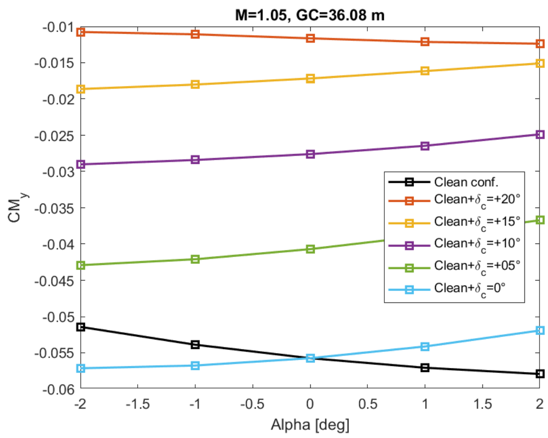

(a) *Canard defections at M=1.05*

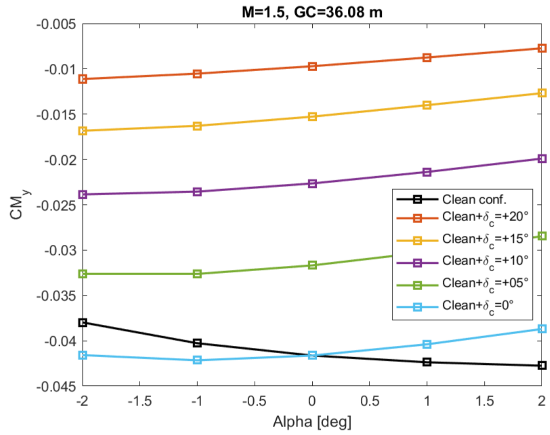

(b) *Canard deflections at M=1.5*

Figure 5.17: Effect of canard with CoG=36.08 m
(transonic regime)

5.3.2 Effect of elevon deflection

The pitching moment coefficient trends, as elevon deflection varies, with respect to the two limit positions of center of gravity are shown in figures 5.18 and 5.19. As already noted in the subsonic regime, the rotation of the elevons do not provide a significant contribution to the stability, thus if the aircraft is stable or unstable with undeflected control surfaces, it continues to be so with the elevons deflected also in these new flight conditions.

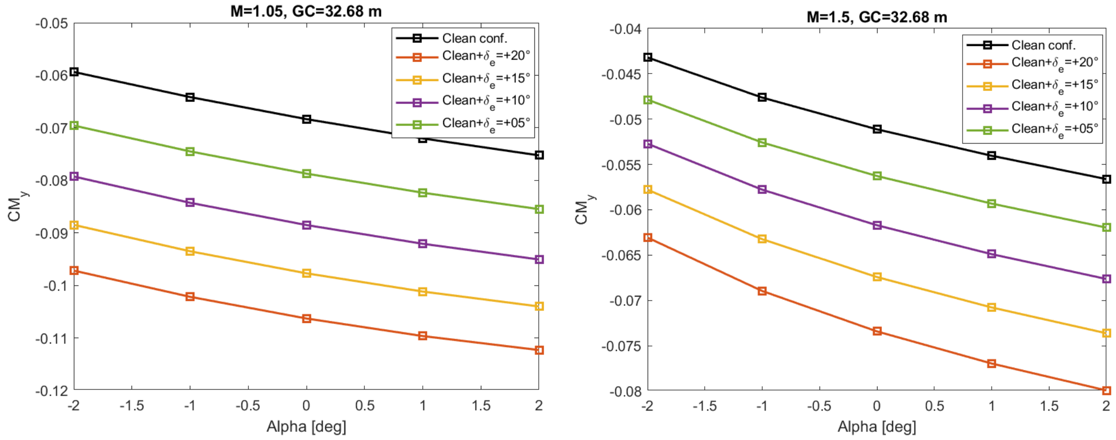

(a) *Elevon defections at M=1.05*　　(b) *Elevon deflections at M=1.5*

Figure 5.18: Effect of elevon with CoG=32.68 m
(transonic regime)

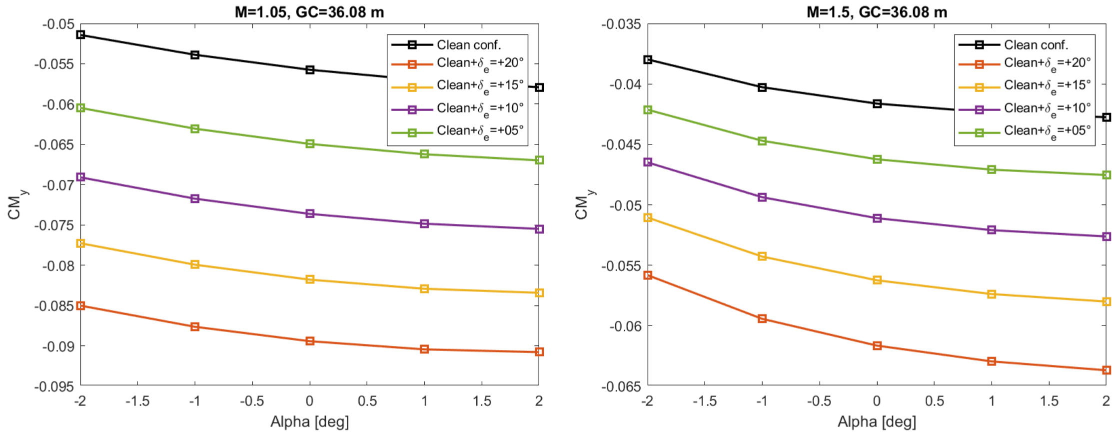

(a) *Elevon defections at M=1.05*　　(b) *Elevon deflections at M=1.5*

Figure 5.19: Effect of elevon with CoG=36.08 m
(transonic regime)

5.3.3 Effect of body-flap deflection

The deflection of body-flap provides a positive contribution to the stability, particularly when the rotations are great. As previously seen, the clean configuration at M=1.05 and M=1.5 with respect to the two limit positions of center of gravity is already stable or nearly stable, thus the rotation of these surfaces allows to further stabilize the aircraft (see figures 5.20 and 5.21).

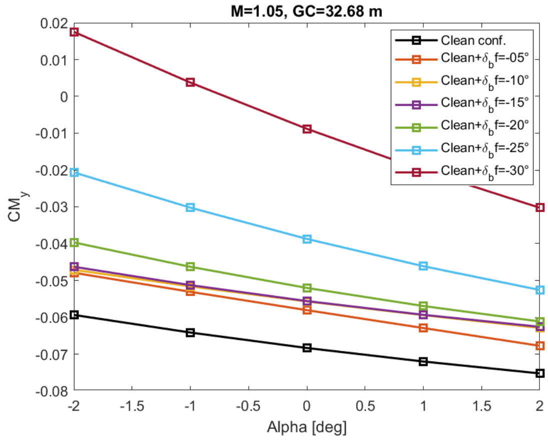

(a) *Body-flap defections at M=1.05*

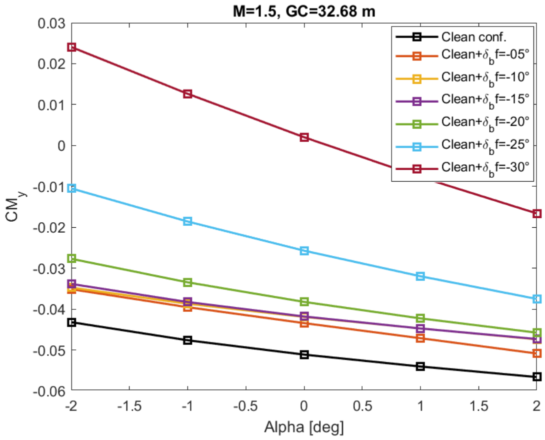

(b) *Body-flap deflections at M=1.5*

Figure 5.20: Effect of body-flap with CoG=32.68 m (transonic regime)

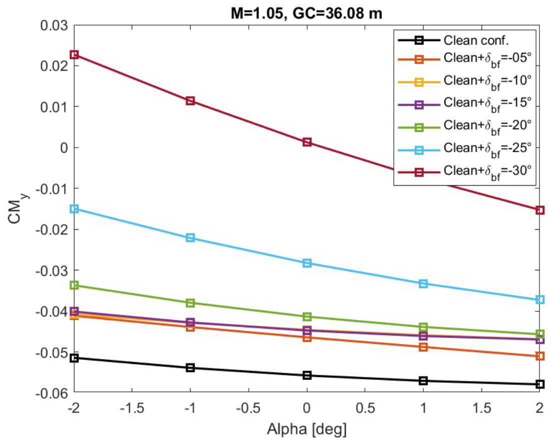

(a) *Body-flap defections at M=1.05*

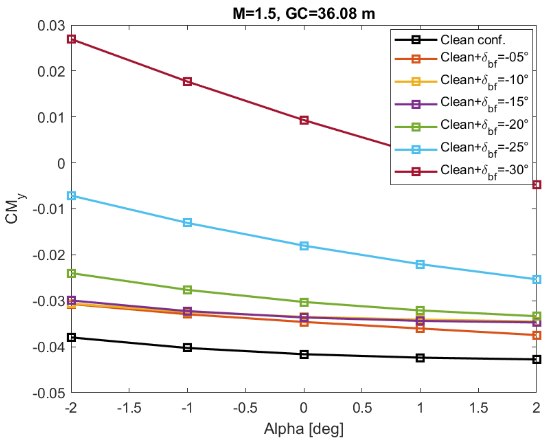

(b) *Body-flap deflections at M=1.5*

Figure 5.21: Effect of body-flap with CoG=36.08 m (transonic regime)

5.4 Supersonic regime

The analysis of the supersonic regime is done considering as reference flight conditions M=3 and M=5, wich is the speed of cruise. In figure 5.22 it can be noted that the continuous lines related to the M=3 condition have different trends, the black curve with CoG=32.68 m has a negative slope, thus the configuration can be considered stable, while the configuration with the further back center of gravity seems to be neutrally stable. The discontinuous lines are instead associated to the cruise condition, the clean configuration with the further back position of center of gravity is unstable or at best neutrally stable, while the curve related to the CoG=32.68 m has a slight negative slope, and thus it is stable.

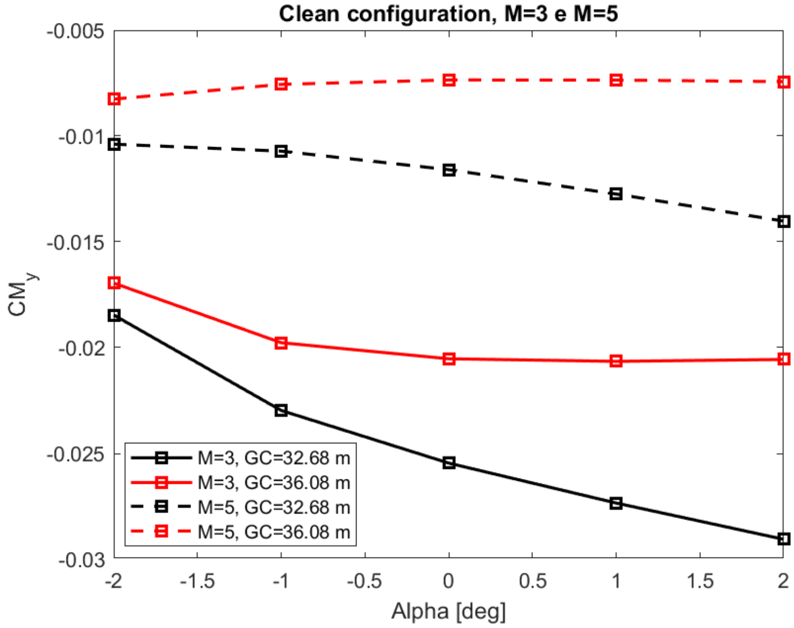

Figure 5.22: Pitching moment coefficeint
vs AoA at M=3 and M=5

5.4.1 Effect of canard deflection

The negative effect on stability of the canard causes a slope reduction of the curves related to the pitching moment coefficient with respect to the CoG=32.68 m, as we can see in figure 5.23, but the configuration continues to be stable or nearly stable. On the contrary in figure 5.24 it can be noted that the addition of canard and its deflections further destabilizes the aircraft that is already neutrally stable or unstable because of the further back position of center of gravity.

5.4.2 Effect of elevon deflection

The effect of elevons deflection on stability is not very important. In figure 5.25 it can be seen that the stable configuration with undeflected control surfaces and with CoG=32.68 m, remains stable also after the rotation of these surfaces. In figure 5.26 there are instead the curves related to the CoG=36.08 m and it can be noted that the trend of them do not change very much but the aircraft tends to be stabilized as the elevon deflection increases.

5.4.3 Effect of body-flap deflection

The positive effect of body-flap on stability can be observed also in these new flight conditions. The deflection of these surfaces allows to stabilize the aircraft in almost all cases for both positions of center of gravity (see figures 5.27 and 5.28).

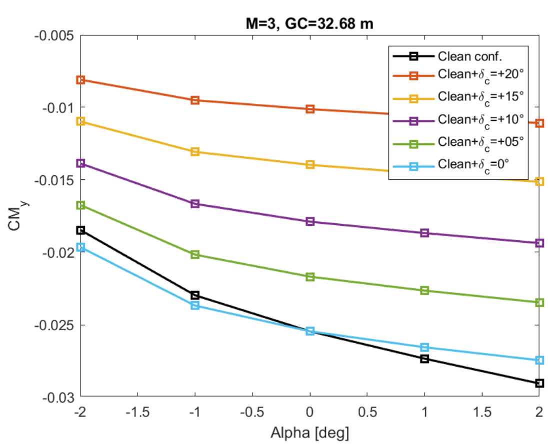

(a) *Canard defections at M=3*

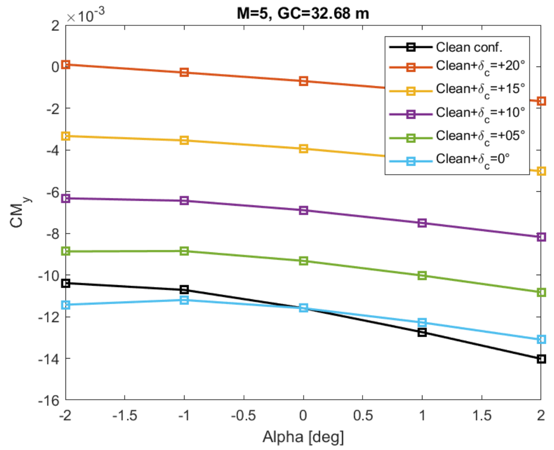

(b) *Canard deflections at M=5*

Figure 5.23: Effect of canard with CoG=32.68 m (supersonic regime)

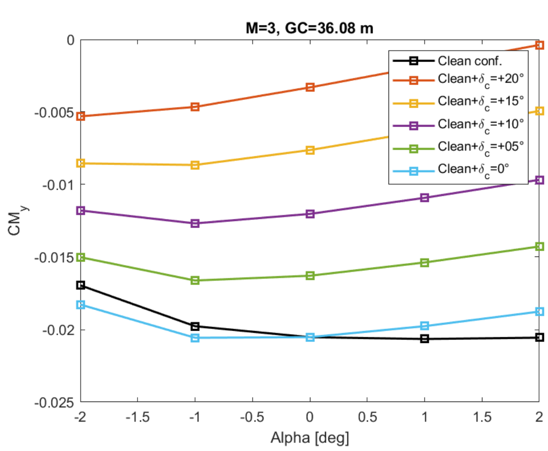

(a) *Canard defections at M=3*

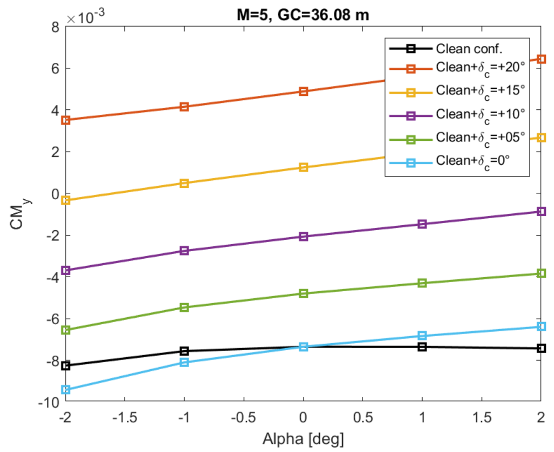

(b) *Canard deflections at M=5*

Figure 5.24: Effect of canard with CoG=36.08 m (supersonic regime)

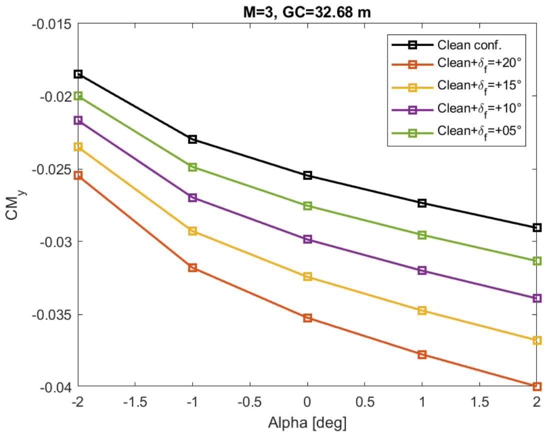

(a) *Elevon defections at M=3*

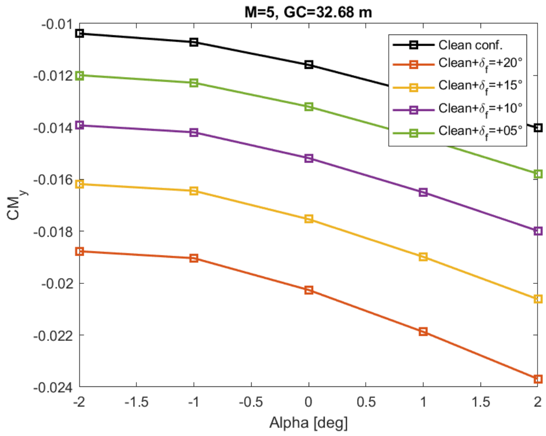

(b) *Elevon deflections at M=5*

Figure 5.25: Effect of elevon with CoG=32.68 m (supersonic regime)

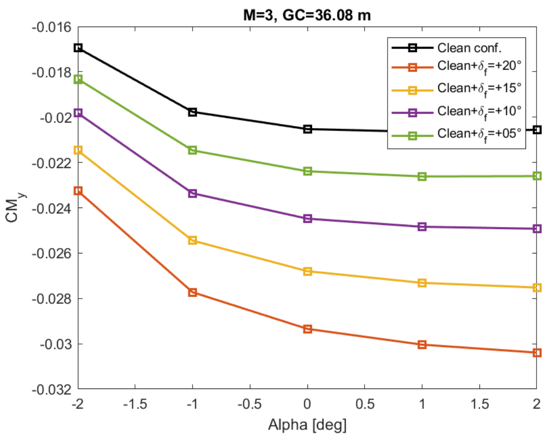

(a) *Elevon defections at M=3*

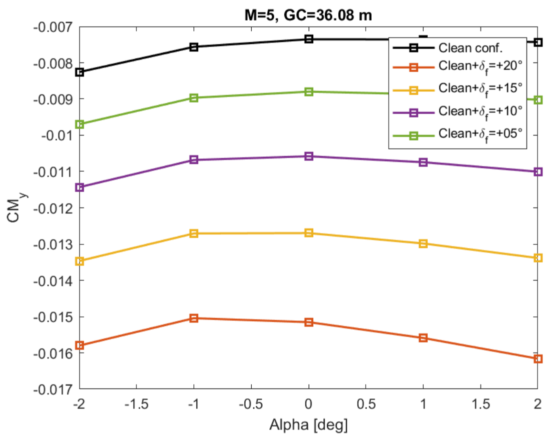

(b) *Elevon deflections at M=5*

Figure 5.26: Effect of elevon with CoG=36.08 m (supersonic regime)

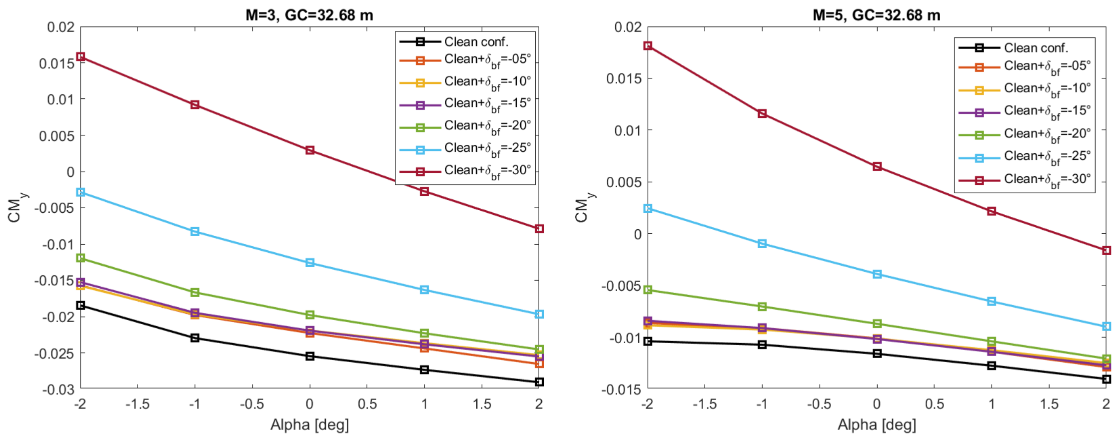

(a) *Body-flap defections at M=3* (b) *Body-flap deflections at M=5*

Figure 5.27: Effect of body-flap with CoG=32.68 m (supersonic regime)

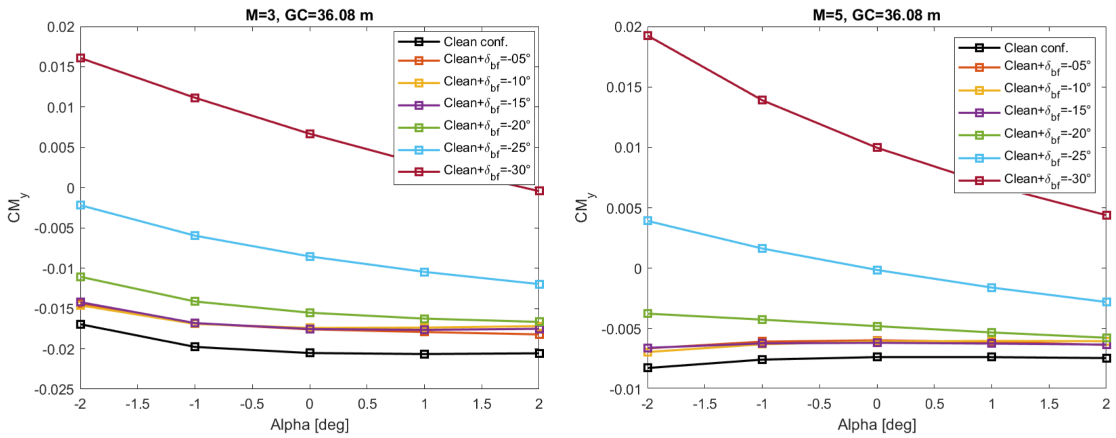

(a) *Body-flap defections at M=3* (b) *Body-flap deflections at M=5*

Figure 5.28: Effect of body-flap with CoG=36.08 m (supersonic regime)

Chapter 6

Trim analysis

6.1 Trim condition

The trim condition occurs when the aircraft is in a balanced flight phase, thus it is not maneuvering, and if the angular speeds are zero it experiences a uniform translational motion with a certain slope (γ) of the trajectory. All forces and moments acting on the aircraft have to satisfy the translation and rotation equilibrium equations, in particular in this discussion only symmetrical longitudinal flight is considered and thus only three equations are used. A simplified scheme of all forces acting on the plane that are lift (L), drag (D), thrust (T) and weight (W), is shown in figure 6.1, and the equations to be respected are reported in the system (6.1), the first two impose the equilibrium to translation and they are written in the wind axes, so in the directions respectively parallel and perpendicular to the velocity vector, while the third is the equilibrium relation to the rotation around the center of gravity.

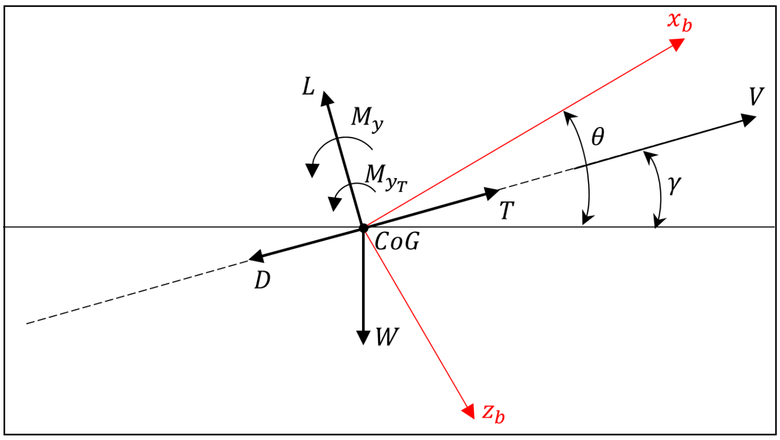

Figure 6.1: Scheme of forces and moments

$$\begin{cases} L = Wcos(\gamma) \\ T - D = Wsin(\gamma) \\ M_y + M_{y_T} = 0 \end{cases} \tag{6.1}$$

It is supposed that the controls are locked, thus for each trim condition there is a combination of control surface deflections that guarantee the balanced flight. The goal of this trim analysis is to determine the deflections necessary in some Mach flight conditions, which are then useful for estimating the power budget required by the mobile surfaces in different phases of the mission profile.

Theoretically, the flight and control parameters that define a trim condition might be calculated by the solution of the system (6.1), indeed the quantities in the equations depend on all these variables, i.e., flight speed and altitude, angle of attack, throttle, and all control surface deflections. Generally, in the search of trim points some of these variables are assigned and others remain unknown, thus if the quantities were expressed explicitly as a function of these variables there would be a system of three equations and some unknowns.

However, in this discussion it has been decided to take a simplified approach considering also the available data that can be used. It is assumed that the lift and the thrust are always able to balance the weight and drag of the aircraft, thus only the rotation equilibrium around the center of gravity is considered as a simplified trim condition. In addition, it is noted that in the (6.1) for the determination of the total moment around the y-axis there is a term depending on thrust. This is because the thrust vector will probably be distant Δz from the x-axis and thus it generates a pitching moment contribution, as was also the case for the STRATOFLY MR3. In the following analysis this contribution is neglected and the trim condition in dimensionless form consists in having zero pitching moment coefficient. As seen in the aerodynamic characterization chapter, this coefficient can be obtained as the sum of more contributions, one related to the clean configuration, and others associated to each control surface deflection, thus the equation to satisfy is the (6.2).

$$C_{M_y} = C_{M_{clean}} + \Delta C_{M_{canard}} + \Delta C_{M_{elevon}} + \Delta C_{M_{BF}} = 0 \tag{6.2}$$

Finally, it is noted that in the search of trim conditions the rudders' deflections are not considered.

In this trim analysis, it is imposed another important constrain to be respected, which consists in having stability around the equilibrium conditions. Therefore, the stability analysis previously done is very useful, and the same reference flight conditions seen there are used also for the trim. In chapter 6 it was noted how the curves of the pitching moment coefficient change as the control surfaces deflections and the center of gravity position vary, and it can be understood that there are different possible combinations of all these variables which allow to respect the condition (6.2), and thus there can be more trim points for each Mach flight condition. The stability constrain helps to reduce the number of possible solutions, and in addition to this another assumption regarding the position of center of gravity is made. Until now two limit positions, within which the center of gravity should fall, were considered, from now on instead a precise location is fixed for each flight condition, in particular it is used the further back point for the subsonic phases, the further forward one for the supersonic phases, and an intermediate position for the transonic regime. This choice is made by observing the shift of the center of gravity of the STRATOFLY MR3 [8].

Taking into account what has just been said, the trim reference points will be determined in the following conditions.

- Subsonic regime with CoG=36.08 m, M=0.5 and M=0.8
- Transonic regime with CoG=34.38 m, M=1.05 and M=1.5
- Supersonic regime with CoG=32.68 m, M=3 and M=5

Considering these conditions, from the stability analysis (see chapter 6) the clean configuration of the aircraft results to be unstable in the subsonic regime, nearly stable in the transonic one and stable in the supersonic phases. However, the deflections of control surfaces must be added to the clean configuration and only some values of them are selected to always guarantee stable trim points. From this point of view, it is remembered that from the stability analysis the effect of control surfaces on longitudinal static stability are:

- CANARD $\longrightarrow$ NEGATIVE EFFECT
- ELEVON $\longrightarrow$ NO SIGNIFICANT EFFECT
- BODY-FLAP $\longrightarrow$ POSITIVE EFFECT

6.2 Trim points

The trim points found for each reference flight condition are reported below, they are defined by the angle of attack and the deflection of canard, elevons and body-flaps. Furthermore, the considerations made for the determination of the trim are shown in detail only for the subsonic case with M=0.5, because the same are repeated also for the other points.

6.2.1 M=0.5 and CoG=36.08 m

In this flight condition the clean configuration of the STRATOFLY MR5 is unstable (see section 5.2). Considering the purpose of finding a stable trim point, firstly the deflection of body-flaps is added because it guarantees a positive effect on stability. The deflections equal to -30°, -25° and -20° are considered, as indicated in the figures 6.2, 6.3 and 6.4, where the pitching moment coefficient curves are shown for each position of body-flaps and as function of canard deflection, which instead has a negative effect on stability. It can be noted that the configuration continues to be unstable with the deflection of -20°, while there are stable trends with the greater rotations in modulus. However, the deflection of -30° is considered for the next steps because it ensures grater stability, and the canard position of 5° is excluded.

Once the rotation of body-flaps has been fixed, the deflection of elevons that instead do not significantly affect the stability, is added. In particular, as indicated in figure 6.5, it is necessary that the curves translate downwards to have $C_{M_y} = 0$, and find a trim point, thus positive deflections of elevons must be considered.

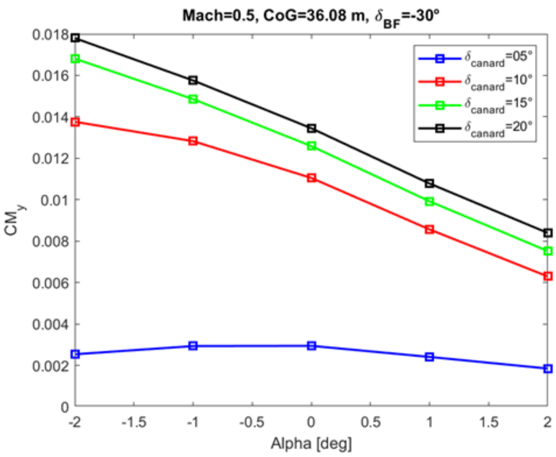

Figure 6.2: C_{M_y} vs AoA with δ_{BF} =-30°

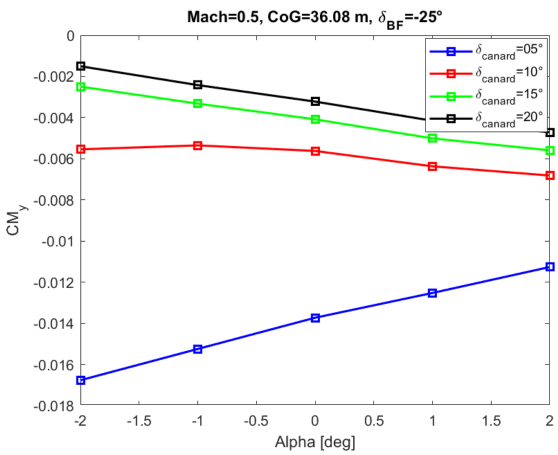

Figure 6.3: C_{M_y} vs AoA with δ_{BF} =-25°

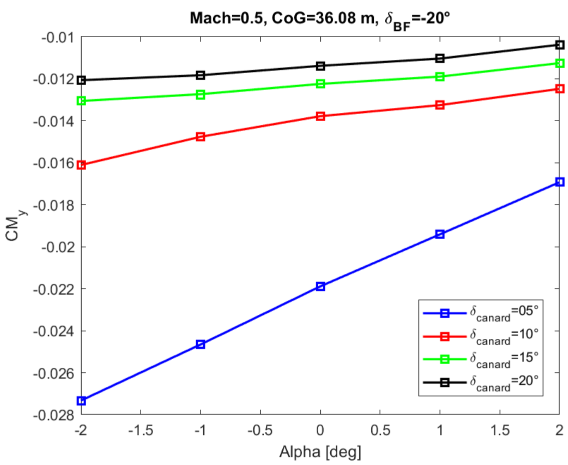

Figure 6.4: C_{M_y} vs AoA with δ_{BF} =-20°

Another variable to consider is the deflection of canard, in the graph of figure 6.5, it can be observed that each curve is associated to different rotations and all of them can intercept the condition CMy=0 with the addition of the elevons, thus there can be different possible trim solutions. However, only one deflection is selected, possibly favoring the smallest ones; in this case the rotation of 15° of the canard is chosen, while the only deflection of elevons that ensures the trim condition is that of 5°, as can be seen in figure 6.6.

Once the deflections of control surfaces have been determined, the last variable to calculate is the angle of attack that completely defines the trim point, indicated with a red circle in the graph of figure 6.7, where all the quantities of the reference trim condition found are also shown.

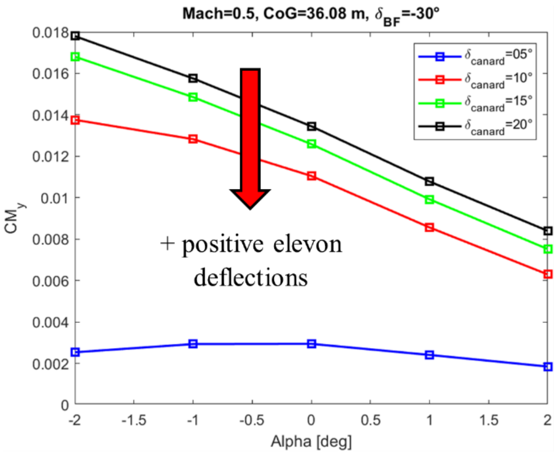

Figure 6.5: Effect of elevon deflections

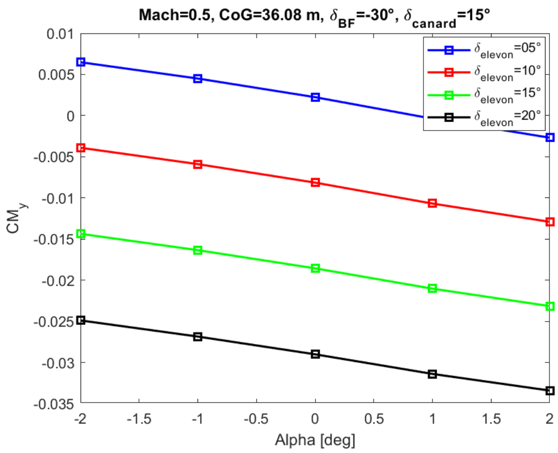

Figure 6.6: C_{M_y} vs AoA and δ_{elevon}

As regards the other flight conditions, only the selected final trim solutions are reported because the arguments made are similar to those just seen.

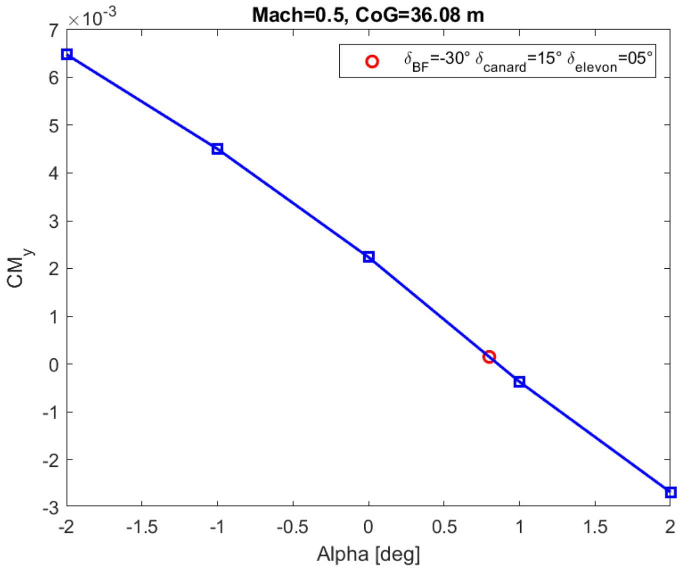

Parameter	Value
M	0.5
δ_{BF}	-30°
δ_{canard}	15°
δ_{elevon}	5°
α_{trim}	0.8°

Figure 6.7: Reference trim point at M=0.5

6.2.2 M=0.8 and CoG=36.08 m

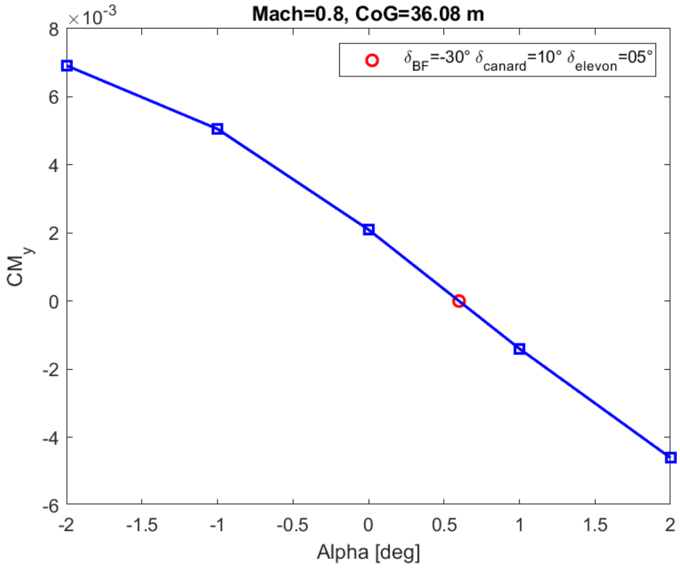

Parameter	Value
M	0.8
δ_{BF}	-30°
δ_{canard}	10°
δ_{elevon}	5°
α_{trim}	0.6°

Figure 6.8: Reference trim point at M=0.8

6.2.3 M=1.05 and CoG=34.38 m

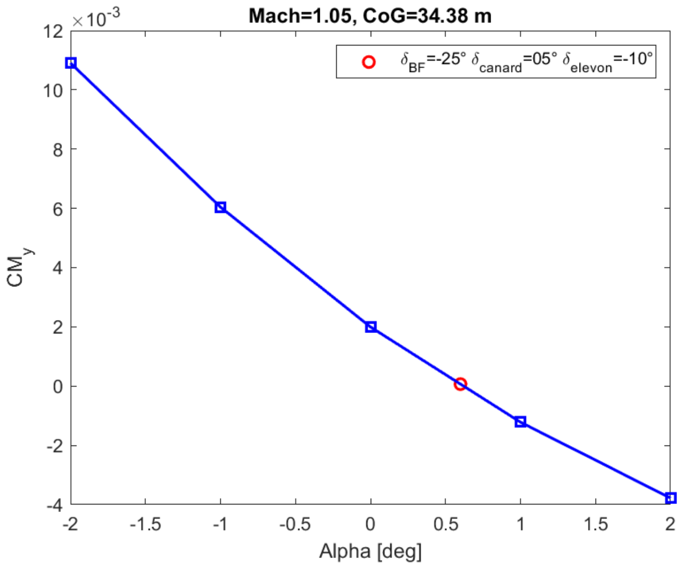

Parameter	Value
M	1.05
δ_{BF}	-25°
δ_{canard}	5°
δ_{elevon}	-10°
α_{trim}	0.6°

Figure 6.9: Reference trim point at M=1.05

6.2.4 M=1.5 and CoG=34.38 m

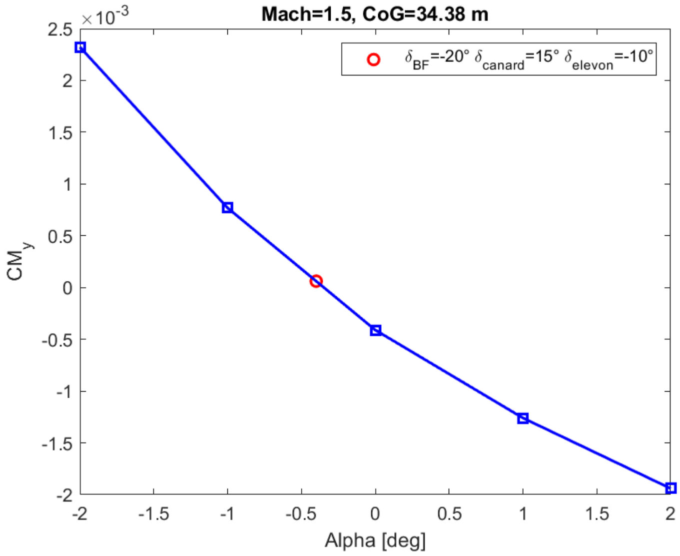

Parameter	Value
M	1.5
δ_{BF}	-20°
δ_{canard}	15°
δ_{elevon}	-10°
α_{trim}	-0.4°

Figure 6.10: Reference trim point at M=1.5

6.2.5 M=3 and CoG=32.68 m

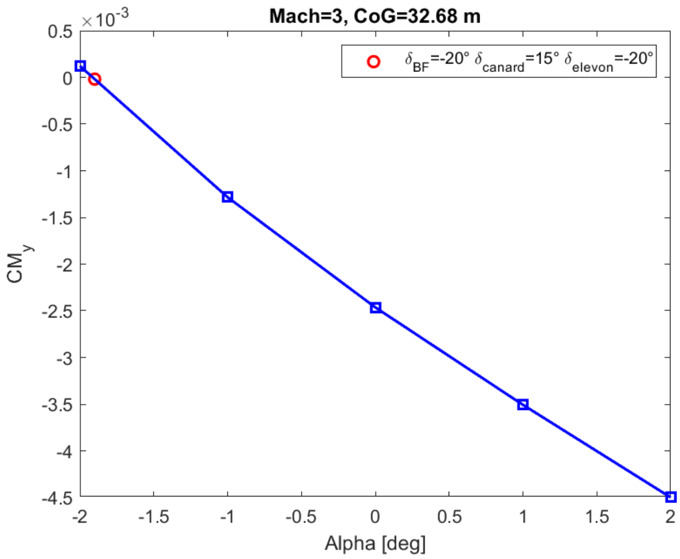

Parameter	Value
M	3
δ_{BF}	-20°
δ_{canard}	15°
δ_{elevon}	-20°
α_{trim}	-1.9°

Figure 6.11: Reference trim point at M=3

6.2.6 M=5 and CoG=32.68 m

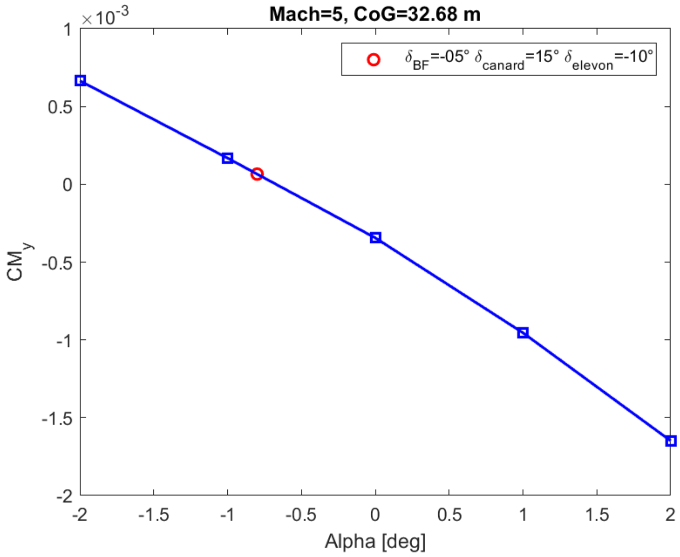

Parameter	Value
M	5
δ_{BF}	-5°
δ_{canard}	15°
δ_{elevon}	-10°
α_{trim}	-0.8°

Figure 6.12: Reference trim point at M=5

Chapter 7

Actuation system sizing

The preliminary design of a FCS also includes the actuation system definition, as mentioned in the introduction chapter. In this thesis work the architecture of the flight control system is not defined in terms of distribution of power supply and flight control computers, but this discussion is limited only to a preliminary estimate of the required actuators and their weight.

The actuators are the devices that lead to move the control surfaces. Today there are different types of them such as hydraulic servo actuator (HSA), electromechanical actuator (EMA) and electro-hydrostatic actuator (EHA). A simplified scheme of these devices is shown in figure 7.1, taken from the reference [12].

The HSAs are the most traditional devices that use a servo valve which receives an electric signal in input and allows to regulate the flows of oil under pressure that act on the hydraulic actuator, finally this last element converts the hydraulic energy into mechanical energy for the movement of the surfaces. This solution is typically used in the fly-by-wire actuation systems, where most of the mechanical connections between pilot controls and surfaces are replaced with an electrical interface, but there is mainly a hydraulic transmission of power, so a fluid under pressure is used.

In recent years there has been a further technological evolution aimed at the development of more/all electric aircraft which has led to the so-called power-by-wire actuation system. The way in which power is transmitted to the command changes compared to the actuation system previously mentioned, the power is transported in wires and the hydraulic connections are eliminated. This aspect has several advantages such as increased safety and reliability due to the absence of flammable hydraulic fluids, reduced weight, volume and complexity of power transmission paths, easier maintenance, less costs due to the lack of hydraulic leaks and better diagnostic capability [12]. Furthermore, in the power-by-wire architecture two types of actuators are used, they are the electromechanical actuator (EMA) and the electro-hydrostatic actuator (EHA).

The electro-hydrostatic actuator is a hydraulic actuator that incorporates a pump driven by an electric motor, and unlike the HSAs the power is regulated by the pump and not by the servo-valve, moreover the hydraulic circuit is autonomous and internal to the actuator, thus it received only electrical connections from the outside, eliminating the heavy external hydraulic transmission lines typical of the HSAs.

The electromechanical actuator allows to completely eliminate the hydraulic fluid, in this case there is an electric motor mechanically connected to the surface to be actuated. The EMA can be linear or rotary, in the first case the rotative motion is converted to linear using appropriate mechanisms such as the screw-nut one, and in the connection, there is generally a gearbox, which reduce the rotational speed of the motor as indicated in figure 7.1b [12].

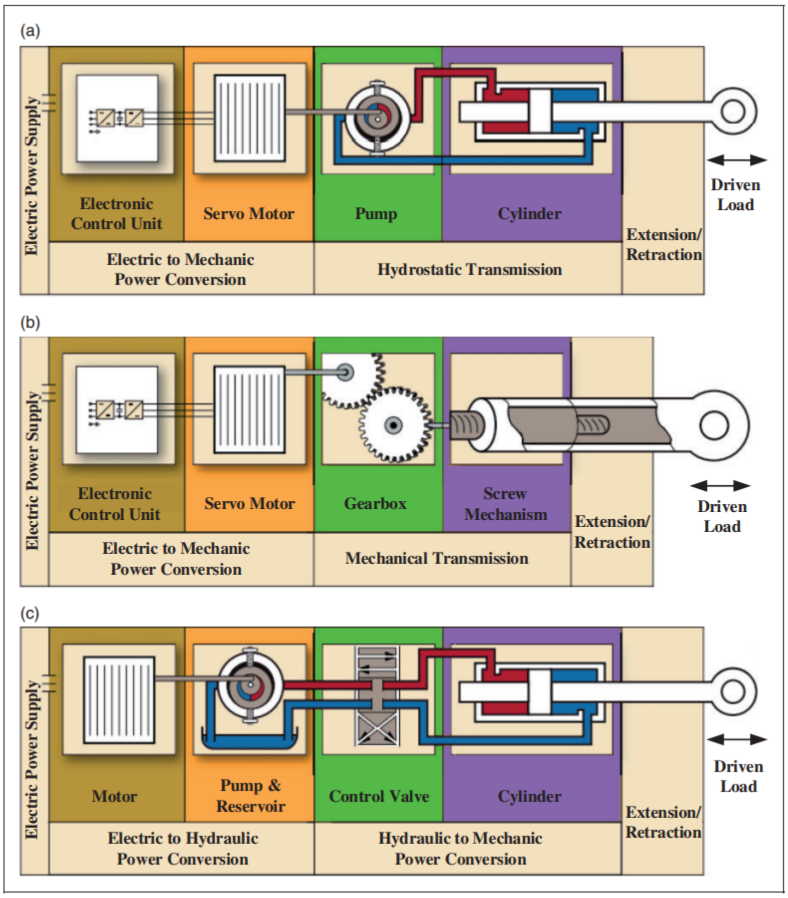

Figure 7.1: Simplified scheme of actuators. (a) EHA, (b) EMA, (c) HSA (Source: [12])

7.1 Hinge moment estimation

The hinge moment develops on any mobile surface, and it is due to the fact that the resultant of the forces acting on the surface does not pass through the hinge axis, so when it is multiplied for an arm, it generates a moment. Different types of forces act on the surface such as aerodynamic forces, weight, friction, and in non-stationary conditions also inertial forces, all of these take part in the generation of a hinge moment that must be opposed so that the control surface is moved and held in a certain position. This task is assigned to the actuators that must also ensure adequate actuation times. Therefore, the choice of the actuators to be used is linked to the actuation power required by the control surfaces, and the most critical condition must be considered. For this case study the reference points seen in the previous chapter, where the trim conditions were estimated, are analyzed; they allow to consider the different flight regimes that are crossed by the aircraft during its mission profile.

The power to be considered for the dimensioning of the actuators is given by the relation (7.1), which is not the only power necessary to move the surface, because it is obtained by multiplying only the hinge moment for the rotational speed, but it is the power that must be rendered available at the FCS.

$$P = \frac{2}{3} M_{hinge} \frac{\omega}{\sqrt{3}} \frac{1}{\eta} \tag{7.1}$$

In this expression there are the actuation system efficiency (η), the desired rotational speed (ω) and hinge moment of the control surface. This last is the most difficult term to estimate, it depends on several parameters such as the deflection and geometric characteristics of the surface, the angle of attack of the aircraft, and the flight conditions. For the estimation of this moment, it is used the approach suggested in the reference [2], in which two different methods are considered depending on the flight conditions, in particular differentiating between Mach numbers lower and greater than two. This distinction is made because, for low Mach numbers, in this case less than two, several studies have been carried out over the years, thus there are traditional approaches in literature that can also be applied in this case study, while for higher Mach numbers these studies are no longer valid, and a new possible method is proposed in reference [2].

7.1.1 Approach used for M<2

For the flight conditions characterized by Mach numbers less than two, there are several studies and suggestions in literature to determine the hinge moment. However, in all cases they are preliminary estimations that can be improved only with more detailed subsequent analyses such as CFD simulations or wind tunnel tests, which are not currently possible. In this treatment the hinge moment is calculated using the relation (7.2).

$$M_{hinge} = \frac{1}{2} \rho V^2 S c C_{M_h} \tag{7.2}$$

In this equation it can be seen that the hinge moment depends on various parameters, such as the flight conditions through the speed and air density, which is related to the flight altitude, the geometric characteristics of the surface through its area and chord. In addition, there is the hinge moment coefficient that is the most difficult element to determine. It has been decided to use a method found in the literature to estimate this parameter, which is defined according to the relation (7.3). It can be noted the dependence on both the angle of attack of the aircraft and the deflection of control surface, while the coefficient K_a and K_b depend on the geometry of the surface, and they are estimated considering the curves reported in figure 7.2, taken from the literature. The curves show the trend of these two coefficients as a function of the ratio between the chord of the mobile part and the chord of the entire surface.

$$C_{M_h} = K_a \alpha^\circ + K_b \delta^\circ \tag{7.3}$$

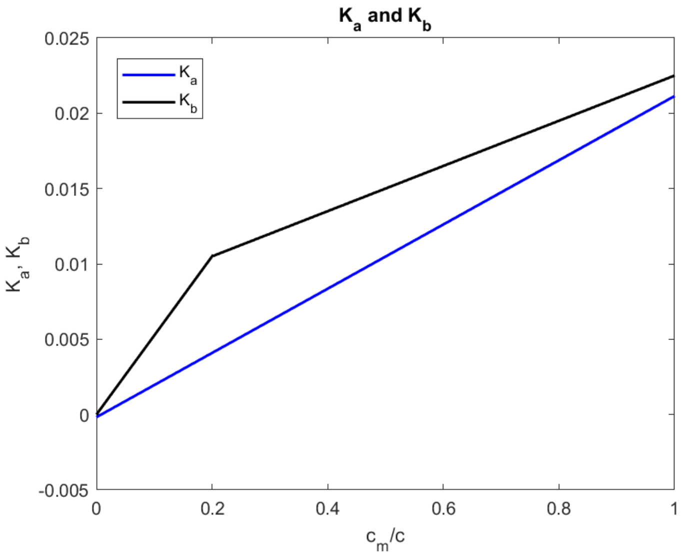

Figure 7.2: K_a and K_b vs c_m/c

Therefore, these two coefficients are determined for each control surface by entering the graph with the respective ratio of the chords. As regards the canard it is considered a unitary ratio because it is a full movable surface. All other data, which are in the relations reported above, are known for each reference trim point, so the hinge moment coefficient and finally the hinge moment can be calculated.

7.1.2 Approach used for M>2

As regards the flight regimes characterized by Mach numbers greater than two, the approach seen in the previous section is no longer valid. Therefore, a simplified method, suggested in reference [2] is used to calculate the hinge moment. It aims to estimate the resultant of the aerodynamic forces acting on the mobile surface, which multiplied by its hinge arm generates the respective moment. This resultant depends on the pressure distribution which develops on the surface. In order to estimate these pressures, it is necessary to consider that when a supersonic flow encounters a deviation, which depends on the geometry of the aircraft in this case, two phenomena can occur: shock waves which slow down the flow and cause an increase in pressure or supersonic expansions, which accelerate the flow and reduce the pressure. When the aircraft configuration is complex several waves or expansions can occur starting from the nose of the plane up to the mobile control surface whose deflection imposes a further deviation to the flow. Therefore, the estimation of the pressure distribution is not easy, but simplified solutions for each control surface are suggested below. The equations used to calculate the characteristics of the flow downstream of the oblique shock wave or the supersonic expansion are reported in the appendix B.

A first simplification consists in the assumption that the mobile surface can be schematized with a flat surface, as indicated in figure 7.3, furthermore it is supposed that the pressures acting on the lower and upper sides of the deflected control surface are constant. With these assumptions the resultant aerodynamic force is given by the relation (7.4) where p is the constant resultant pressure acting on the surface and A is the surface area.

$$F_{surface} = p \cdot A_{surface} \tag{7.4}$$

When the force is known, it is possible to calculate the hinge moment with the equation (7.5) where $c_{h_{surface}}$ is the hinge arm, i.e., the distance between the hinge axis and the point of application of the resulting force, and it is assumed that this is equal to half of the surface chord.

$$M_{h_{surface}} = F_{surface} \cdot c_{h_{surface}} = F_{surface} \cdot \frac{c_{surface}}{2} \tag{7.5}$$

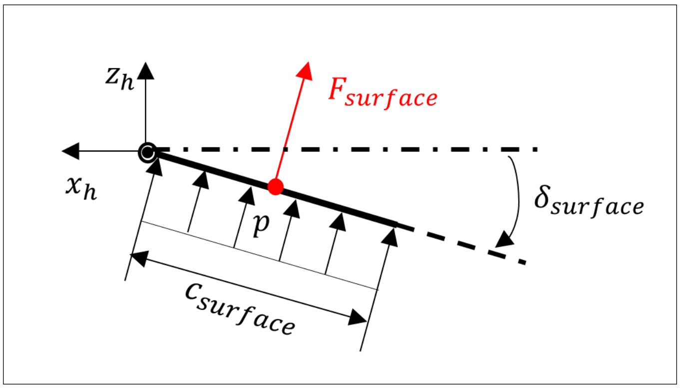

Figure 7.3: Control surface schematized with a flat surface

Body-flap

The body-flap surfaces are positioned on the body of the aircraft, in particular on the top of the integrated nozzle, considering the negative angle of attack that characterized the supersonic trim points to analyze, it is supposed that two oblique shock waves occur, as indicated in figure 7.4: the first one, which depends on the angle of attack at the nose of the aircraft, and the second one, which depends on the deflection of the mobile part, at the beginning of the control surface. Therefore, the equations of the oblique shock theory are applied two times, and the pressure established downstream of the second wave corresponds to the pressure acting on the mobile surface. Finally, the hinge moment of the body-flaps can be calculated using the relations (7.4) and (7.5).

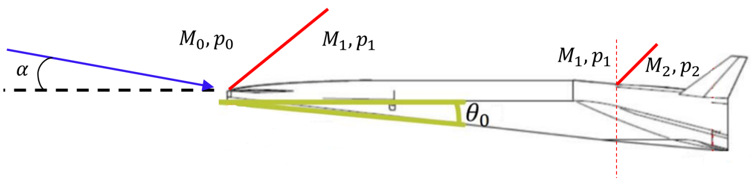

Figure 7.4: Solution considered to determine the pressure distribution on body-flaps

Elevon

The elevon surfaces are positioned at the rear part of the wing, so the flow encounters various deviations following the complex airfoil of the wing before reaching these mobile surfaces. In particular (see figure 7.5) two oblique shock waves are considered at the leading edge, then continuing on the upper side of the wing there is a supersonic expansion when the airfoil diverts the flow downwards, and finally another shock wave occurs in correspondence with the deflection of the elevon, while on the lower side of the aircraft a supersonic expansion is considered at the beginning of the control surface because the elevon has a negative deflection, so it is rotated upwards. In this case the pressure to use in the equation (7.4) to calculate the resultant force is given by the difference between the pressure p_3 and p_5 that act on the upper and lower sides of the elevon.

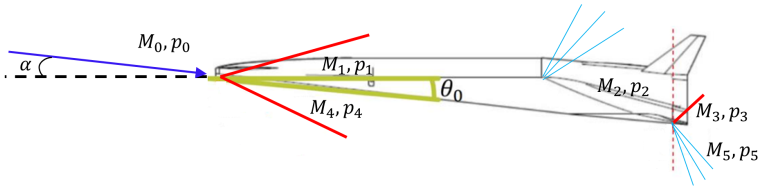

Figure 7.5: Solution considered to determine the pressure distribution on elevons

Canard

The canard is a fully movable surface positioned at the front of the aircraft, thus it is supposed, as simplification, that it is isolated, and when the flow encounters this surface with a positive deflection two phenomena occur: an oblique shock wave on the upper side of the surface and a supersonic expansion on the lower side as indicated in figure 7.6. In this case the deviation imposed on the flow is δ_{eff}, which is given by the relation (7.6) that considers both the deflection of the canard and the orientation of the aircraft with respect to the flow. If this deviation is negative the two phenomena mentioned before are reversed. The total constant pressure acting on the canard is given by the difference between p_1 and p_2 (see figure 7.6).

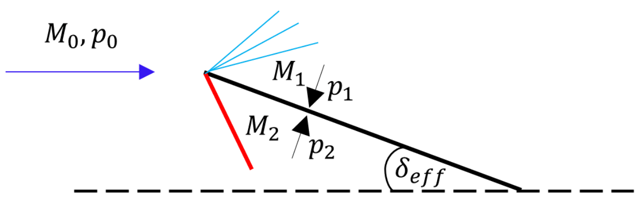

Figure 7.6: Solution considered to determine the pressure distribution on canard

$$\delta_{eff} = AoA + \delta_{canard} \tag{7.6}$$

Rudder

Until now, the rudders were mentioned only in the chapter 3, in the context of the geometric sizing of the control surfaces, and they were not included in the search for the trim conditions. In general, the ruddervetors, present on the V-tail surfaces, affect both the longitudinal and lateral-directional trim because the forces acting on them have a component in both y and z directions. However, it has been decided to follow the same approach used for the STRATOFLY MR3, in which the rudders were considered only for the directional control, furthermore, to have an idea of the deflections required along the mission profile it was supposed to have symmetrical deflections of the surfaces, and for simplicity the deflection was gradually varied from a maximum of 20° at low Mach numbers and a minimum of about 1° or 4° at Mach 8. In this case study a linear trend of the deflection as Mach number varies is assumed as indicated in figure 7.7, considering a maximum value of 20° at Mach 0.3 and a minimum of 2° at Mach 5 in cruise. Therefore, for each trim condition the reference rotation of rudders can be obtained entering in this graph with the respective value of Mach. This deflection is used to calculate the hinge moment, always distinguishing between the cases with M<2 and M>2, and finally the actuation power to get an idea of the necessary actuators for these control surfaces.

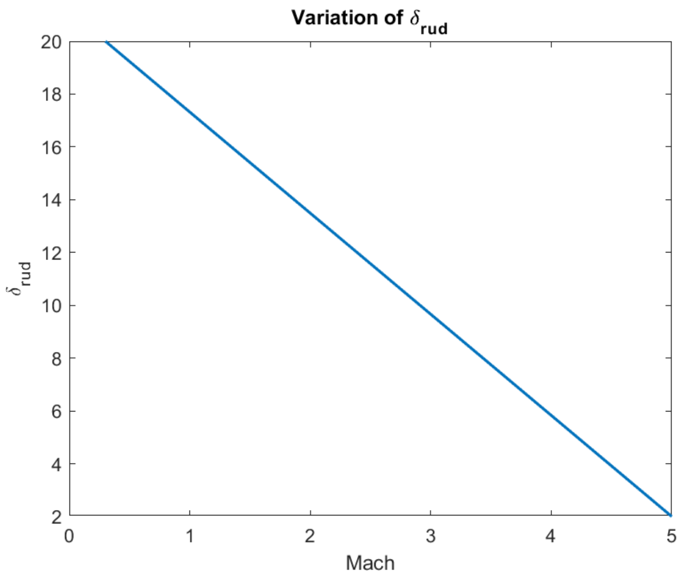

Figure 7.7: Rudder deflection vs Mach number

As regards the flight conditions with M>2, it is supposed that the supersonic flow continues undisturbed until it encounters the deflected rudder, which imposes a deviation. Therefore, this is a situation similar to that seen for the canard, with the generation of an oblique shock wave on one side and a supersonic expansion on the other side. In addition, it is assumed that the two rudders are deflected symmetrically, thus only one surface can be analyzed because the results are the same.

7.2 Actuation power demand

Once the hinge moment has been calculated for each control surface and at each reference trim condition, the actuation power demand can be calculated with the equation (7.1). The results obtained are shown in the tables 7.1, 7.2, 7.3 and 7.4, indicating for each condition the required deflection of the surface and the actuation time considered to reach it starting from the neutral position.

Table 7.1: Power required by body-flap (single surface)

Phase	**AoA [deg]**	δ_{bf} **[deg]**	t_{bf} **[sec]**	P_{bf} **[kW]**
M=0.5	0.8	-30	1	19.4
M=0.8	0.6	-30	1	26.1
M=1.05	0.6	-25	1	11.1
M=1.5	-0.4	-25	1	9.17
M=3	-1.9	-20	2	44.8
M=5	-0.8	-5	2	1.76

Table 7.2: Power required by elevon (single surface)

Phase	**AoA [deg]**	δ_e **[deg]**	t_e **[sec]**	P_e **[kW]**
M=0.5	0.8	5	1	0.11
M=0.8	0.6	5	1	0.14
M=1.05	0.6	-10	1	0.32
M=1.5	-0.4	-10	1	0.42
M=3	-1.9	-20	1.5	3.26
M=5	-0.8	-10	1.5	0.16

The figure 7.8 reports a bar diagram in which it is possible to see the power demand of the entire FCS (see also table 7.5), thus all control surfaces are included for each reference flight condition, and the different contributions of the surfaces are shown. These results, as already mentioned, depend on several factors, among which the deflections and the actuation times considered, the flight altitude and speed, and also the surface size. It can be noted that the surface, which tends to always provide the greatest contribution to the required power, is the canard that is also the largest surface to be moved, and there is an exception at Mach 1.05 because the deflection is the smallest. The surfaces that instead require less power are almost always the elevons. Furthermore, it is noted that the power demand at Mach 5 is about 53 kW, which is lower than in almost all other conditions, and thus considering it as a reference for sizing would be a mistake, although it is the cruise phase. Indeed, the most critical condition is the one at Mach 0.5 with a power peak of 183.1 kW.

Table 7.3: Power required by canard (single surface)

Phase	**AoA [deg]**	δ_c **[deg]**	t_c **[sec]**	P_c **[kW]**
M=0.5	0.8	15	1	61.7
M=0.8	0.6	10	1	36.9
M=1.05	0.6	5	1	5.97
M=1.5	-0.4	15	1	59.8
M=3	-1.9	15	2	35.9
M=5	-0.8	15	2	24.3

Table 7.4: Power required by rudder (single surface)

Phase	**AoA [deg]**	δ_r **[deg]**	t_r **[sec]**	P_r **[kW]**
M=0.5	0.8	19.2	1	10.2
M=0.8	0.6	18.1	1	11.9
M=1.05	0.6	17.1	1	6.58
M=1.5	-0.4	15.4	1	6.53
M=3	-1.9	9.6	1.5	4.03
M=5	-0.8	2	1.5	0.1

7.3 Actuators mass

Once the FCS power demand has been determined, it is possible to preliminary estimate the mass of the actuators needed to move the control surfaces. Firstly, one type of actuator must be selected from those mentioned before. The STRATOFLY MR5 is a more-all electric aircraft, as the MR3, thus the choice is between electromechanical and electro-hydrostatic actuators. Today the EHAs are already in service for primary flight controls, while the EMAs are used more for the secondary ones. Indeed, the latter technology is less mature than the others, especially because of the lack of accumulated knowledge and experience regarding reliability and the risk of failures, health monitoring and thermal management [12]. For this reason the EHAs are selected for this case study.

Finally, the mass of actuators is estimated using the power to weight parameter, of which a reference value taken from literature is considered, and it is defined as the relation (7.7).

$$c = \frac{max(P_{surface})}{M_{actuator}} = 0.25 \quad \frac{kW}{kg} \tag{7.7}$$

Therefore, it is necessary to identify the maximum actuation power required by each control surface, and then the mass of the respective actuators can be estimated with the reverse formula. The results obtained for each single surface are shown in the table 7.6. Finally, the preliminary estimate of the total mass of all actuators is around 1000 kg.

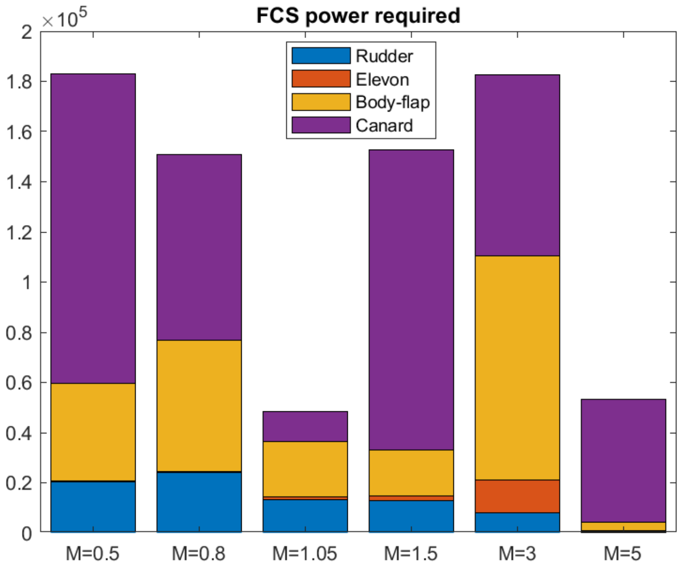

Figure 7.8: FCS power demand

Table 7.5: FCS power required (all surfaces)

Phase	P_{tot} **[kW]**
M=0.5	183.1
M=0.8	150.7
M=1.05	48.56
M=1.5	152.8
M=3	182.5
M=5	53.09

Table 7.6: Single surface actuator mass

Single surface	$M_{actuator}$ **[kg]**
Body-flap	179
Elevon	13
Canard	247
Rudder	48

Chapter 8

Conclusions

The aim of this thesis work is to propose an approach for the preliminary design of the flight control system of a civil aircraft flying at Mach 5 in cruise. This is a very current topic as seen in the introduction chapter, in which it is highlighted the great interest that exists today in the high-speed aircraft, both supersonic and hypersonic. In the past the progress in these technologies has been driven mainly by military applications, but the value of supersonic and hypersonic market has grown in the last decade and it is estimated that it will continue to grow in the coming years also thanks to the strong interest in the return of high-speed civil flight after the last experience dating back to 2003 with the Concorde.

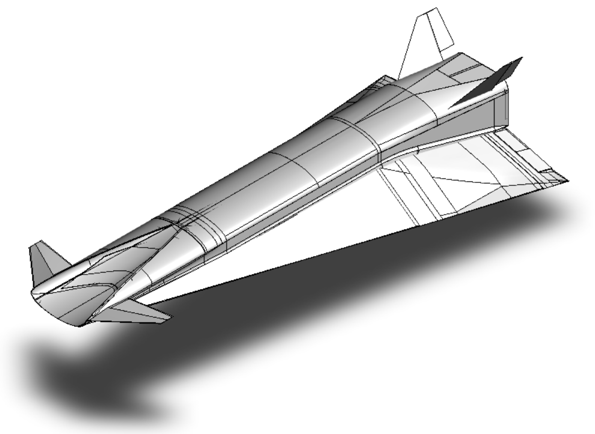

Figure 8.1: STRATOFLY MR5

The case study considered in this thesis is the STRATOFLY MR5 (see figure 8.1) that was born in the H2020 MORE&LESS project funded by the European Union, which aims to analyze the environmental impact of supersonic aviation. At the beginning of this thesis work the available data were few because it was still in the first phases of the design, in which a preliminary external configuration of the MR5 had been defined starting from another aircraft that is the MR3, born in the STRATOFLY project, also funded by the European Union. This is considered as reference aircraft par excellence in this work, furthermore in the steps that are followed for the preliminary sizing of the FCS it is necessary to make some simplifying assumptions, and it is noted that they must be considered in the evaluation of the analyzes and results obtained which mainly aim to have an idea of the orders of magnitude that characterize this system.

The first part deals with the geometric sizing of the control surfaces, i.e. canard, body-flaps, elevons and rudders. It is considered an approach, also commonly used by subsonic conventional aircraft, which exploits the volume coefficients, and typical ratios between the area of the mobile part and the total reference area. In this first phase the known geometric data of the MR3 are already useful because they are a good starting point to define all the geometric characteristics of the new surfaces.

Then, a preliminary aerodynamic characterization of the aircraft is carried out, using in this case an approach specific for this case study. A simplified aerodynamic model, designed for high-speed vehicles, is applied to estimate the aerodynamic coefficients of the clean configuration of the MR5, which consists of the external vehicle layout with undeflected control surfaces. The available aerodynamic database of the MR3 is instead exploited to determine the contributions given by the control surfaces. The data obtained can not be considered particularly correct because of the considered simplifications, but they can represent a starting point to have an idea of the aerodynamic performance of the aircraft and to proceed in the preliminary sizing of the flight control system.

Subsequently, a longitudinal static stability is carried out, exploiting the aerodynamic data previously estimated. From the analysis it is possible to see that the MR5 tends to have some stability problems, as it is very common in high-speed aircraft, in particular, in the subsonic phases there is the tendency to experience greater instability than in the supersonic phases. For these reasons it will most likely be necessary to implement appropriate active control systems. However, these aspects depend on various factors such as the shift along the mission profile of the aerodynamic center and center of gravity, whose values are assumed in this case considering the respective known data relating to the MR3. Therefore, in the future it will be useful to carry out even more detailed analyzes of these phenomena.

In the last part of the thesis, the aerodynamic characterization and the stability analysis are useful to identify some possible trim points, which can be considered to estimate the actuation power required by the FCS in some reference phases of the aircraft mission profile. Again, it is necessary to apply a different approach compared to the subsonic designs, to take into account some phenomena that characterized the high-speed flows, i.e., the oblique shock wave and the supersonic expansion. Finally, it is possible to have an idea of the order of magnitude of the maximum power required by the system, and the mass of actuators needed on board.

Appendix A

Aerodynamic equations

The aerodynamic equations reported in this appendix are taken mainly from the reference [11], but there are some differences due instead to the corrections suggested in the reference [10].

A.1 Lift coefficient

$$C_L = C_{L_0} + C_1 sin(\alpha) + C_2 sin^2(\alpha) \tag{A.1}$$

$$\begin{cases} C_1 = \frac{\pi \cdot AR}{2} - 0.355 \cdot \beta^{0.45} \cdot AR^{1.45} & M \leq 1 \\ C_1 = \frac{\pi \cdot AR}{2} - 0.153 \cdot \beta \cdot AR^2 & M > 1 \text{ and } \beta < \frac{4}{AR} \\ C_1 = \frac{4.17}{\beta} - 0.13 & M > 1 \text{ and } \beta \geq \frac{4}{AR} \end{cases} \tag{A.2}$$

$$\begin{cases} C_2 = 0 & M \leq 1 \\ C_2 = linear\ interpolation\ with\ respect\ to\ \beta & M > 1 \text{ and } \beta < \frac{4}{AR} \\ C_2 = e^{[0.955-(4.35/M)]} & M > 1 \text{ and } \beta \geq \frac{4}{AR} \end{cases} \tag{A.3}$$

Where:

$$\beta = \sqrt{|M^2 - 1|}$$

$$AR = \frac{b^2}{S_{ref}}$$

$$C_{L_0} = from\ the\ database\ of\ MR3,\ clean\ configuration$$

A.2 Drag coefficient

$$C_D = C_{D_0} + C_{D_{0VT}} + C_{D_i} \tag{A.4}$$

Where:

$$C_{D_0} = zero\text{-}lift\ body\ drag$$

$$C_{D_{0VT}} = \textit{zero-lift V-tail drag}$$

$$C_{D_i} = \textit{induced drag}$$

A.2.1 Induced drag

$$\begin{cases} C_{D_i} = 1.3 \cdot C_L \cdot \tan(\alpha + 4) & M \leq 1 \\ C_{D_i} = \textit{is evaluated through interpolation for} & 1 < M < 3 \\ C_{D_i} = 1 \cdot C_L \cdot \tan(\alpha + 2) & M \geq 3 \end{cases} \tag{A.5}$$

A.2.2 Zero-lift body drag

$$C_{D_0} = C_{D_{PB}} + C_{D_{FB}} + C_{D_{BB}} \tag{A.6}$$

- **Body pressure drag** ($C_{D_{PB}}$)

$$\begin{cases} C_{D_{PB}} = 0 & M \leq 0.8 \\ C_{D_{PB}} = \textit{linear interpolation with respect to M from} & \\ \qquad C_{D_{PB}} = 0 \textit{ at M=0.8 to} & 0.8 < M < 1.2 \\ \qquad C_{D_{PB}} = C_{D_{PB}} \textit{ at M=1.2} & \\ C_{D_{PB}} = 1.8 \cdot cp \cdot \frac{\pi}{4} \cdot \frac{1}{S_{ref}} \cdot d^2 & M \geq 1.2 \end{cases} \tag{A.7}$$

Where:

$$d = \sqrt{\frac{S_\pi}{\pi}}$$

$$cp = \frac{2 \cdot \theta}{\beta}$$

$$\theta = \frac{\pi}{2} - \Lambda_{wing}$$

- **Body friction drag** ($C_{D_{FB}}$)

$$C_{D_{FB}} = \frac{0.455}{[\log_{10}(Re_b)]^{2.58} \cdot \frac{1}{(1+0.310 \cdot M^2)^{0.37}} \cdot S_{wet}/S_{ref}} \qquad \forall M \tag{A.8}$$

Where:

$$Re_b = \rho M a \frac{MAC}{\mu}$$

- **Body bluntness drag** ($C_{D_{BB}}$)

$$\begin{cases} C_{D_{BB}} = 0 & M \leq 0.8 \\ C_{D_{BB}} = \textit{linear interpolation with respect to M from} & \\ \qquad C_{D_{BB}} = 0 \textit{ at M=0.8 to} & 0.8 < M < 1 \\ \qquad C_{D_{BB}} = C_{D_{BB}} \textit{ at M=1} & \\ C_{D_{BB}} = \frac{\pi \cdot r^2_{NOSE}}{S_{ref}} & M \geq 1 \end{cases} \tag{A.9}$$

Where:

$$r^{0.5}_{NOSE} = \frac{1820 \cdot (\frac{\rho}{\rho_{SL}})^{1/2} \cdot (M_{MAX} a 10^{-4})^{3.15}}{\epsilon_{SKIN} \cdot (\frac{T_{LE}}{1000})^4}$$

$$h_{cruise} = 30km$$

$$\rho(h_{cruise})$$

$$a(h_{cruise})$$

$$M_{MAX} = 5$$

$$\epsilon_{SKIN} = 0.8$$

$$T_{LE} = T_{cruise}(1 + 0.2M^2_{cruise}) = 1359K = 2446°R$$

A.2.3 Zero-lift V-tail drag

$$C_{D_{0VT}} = C_{D_{PVT}} + C_{D_{FVT}} + C_{D_{BVT}} \tag{A.10}$$

- **V-tail pressure drag** ($C_{D_{P_{VT}}}$)

$$\begin{cases} C_{D_{PVT}} = 0 & M \leq 0.8 \\ C_{D_{PVT}} = \textit{linear interpolation with respect to M from} & \\ \qquad C_{D_{PVT}} = 0 \textit{ at M=0.8 to} & 0.8 < M < 1 \\ \qquad C_{D_{PVT}} = C_{D_{PVT}} \textit{ at M=1} & \\ C_{D_{PVT}} = 3.4(\frac{t}{c})^{\frac{5}{3}}_{VT} \frac{S_{VT}}{S_{ref}} cos^2(\Lambda_{VT}) & M = 1 \\ C_{D_{PVT}} = 6(\frac{t}{c})^2_{VT} \frac{1}{\beta} \frac{S_{VT}}{S_{ref}} & M > 1 \end{cases} \tag{A.11}$$

- **V-tail friction drag** ($C_{D_{FVT}}$)

$$C_{D_{FVT}} = 0.455 \frac{\left[1 + 2(\frac{t}{c})_{VT}\right]\left[\frac{(S_{wet})_{VT}}{S_{ref}}\right]}{(log_{10} Re_{VT})^{2.58}(1 + \frac{\gamma - 1}{2} M^2)^{0.467}} \qquad \forall M \tag{A.12}$$

Where:

$$Re_{VT} = \rho M a \frac{MAC_{VT}}{\mu}$$

- **V-tail bluntness drag** ($C_{D_{BVT}}$)

$$\begin{cases} C_{D_{BVT}} = 0 & M \leq 0.8 \\ C_{D_{BVT}} = linear\ interpolation\ with\ respect\ to\ M\ from & \\ \qquad C_{D_{BVT}} = 0\ at\ M{=}0.8\ to & 0.8 < M < 1 \\ \qquad C_{D_{BVT}} = C_{D_{BVT}}\ at\ M{=}1 & \\ C_{D_{BVT}} = \frac{8}{3}\frac{r_{LE_{VT}} b_V}{S_{ref}} cos^2(\Lambda_V) & M \geq 1 \end{cases} \tag{A.13}$$

Where:

$$r_{LE_{VT}} = (0.725cos^{1.2}\Lambda_V)^2 r_{NOSE}$$

Appendix B

Oblique shock wave and supersonic expansion

B.1 Oblique shock wave

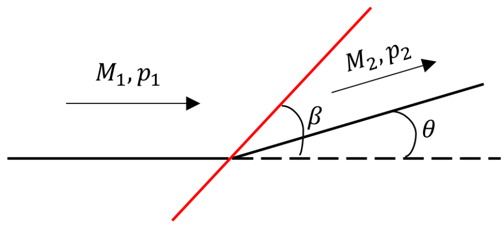

Figure B.1: Oblique shock wave

- **Relation** $\theta - \beta - M$

$$\tan(\theta) = \frac{2}{\tan(\beta)}\left[\frac{M_1^2(sin\beta)^2 - 1}{M_1^2(\gamma + cos2\beta) + 2}\right] \tag{B.1}$$

- **Relation between downstream and upstream pressures**

$$p_2 = p_1\left(1 + \frac{2\gamma(M_1^2(sin\beta)^2 - 1)}{\gamma + 1}\right) \tag{B.2}$$

- **Relation between downstream and upstream Mach numbers**

$$M_2 = \frac{1}{sin(\beta - \theta)}\sqrt{\frac{2 + (\gamma - 1)M_1^2(sin\beta)^2}{2\gamma M_1^2(sin\beta)^2 - (\gamma - 1)}} \tag{B.3}$$

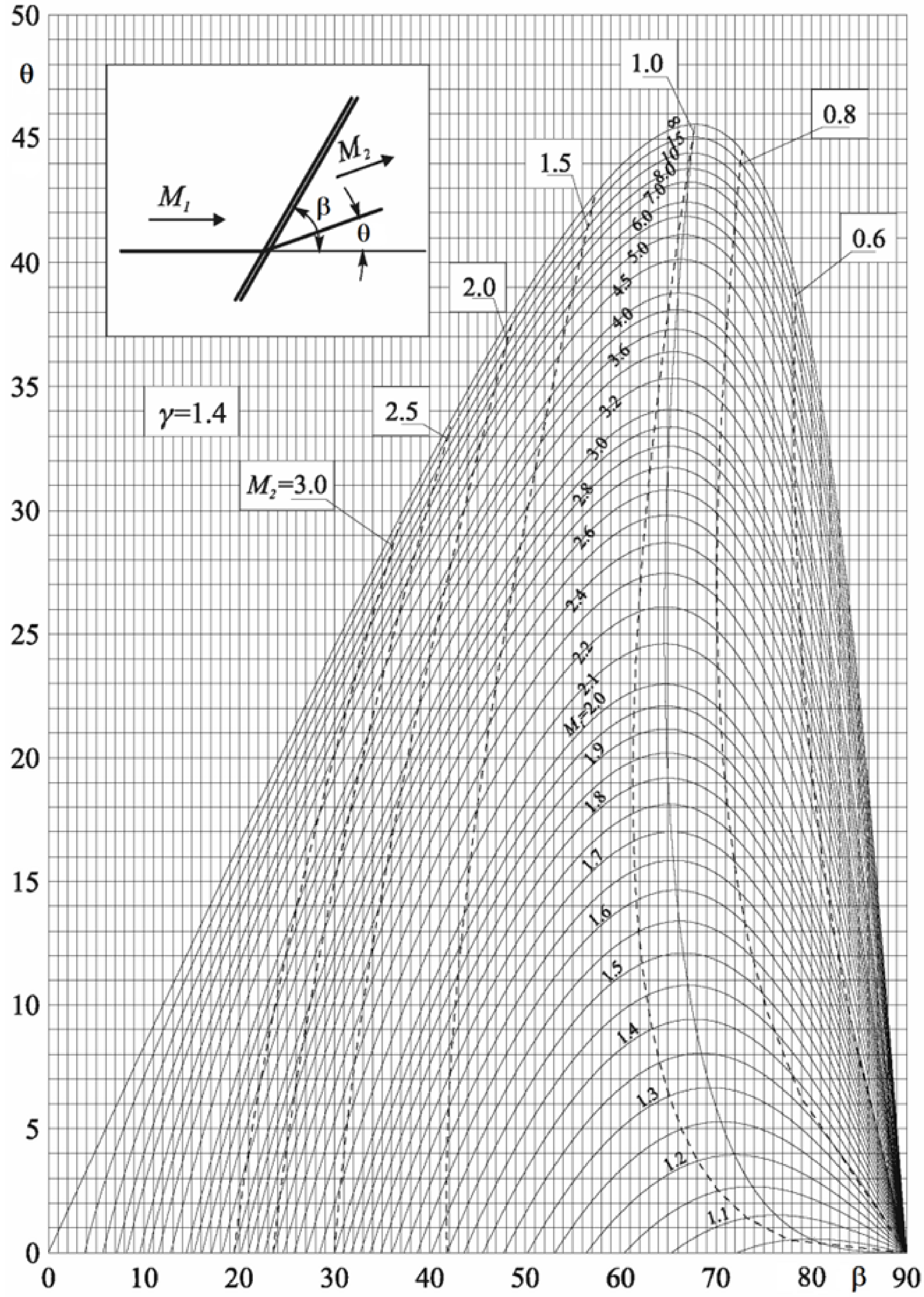

Figure B.2: $\theta - \beta - M$ diagram

B.2 Supersonic expansion

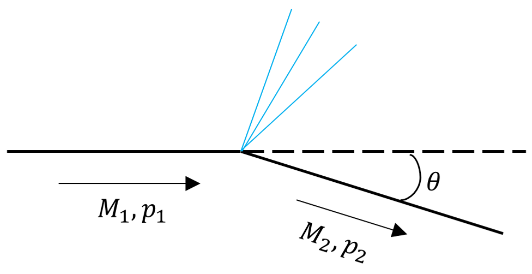

Figure B.3: Supersonic expansion

- **Prandtl-Meyer function**

$$\nu(M) = \sqrt{\frac{\gamma+1}{\gamma-1}} tan^{-1}\left[\sqrt{\frac{\gamma-1}{\gamma+1}(M^2-1)}\right] - tan^{-1}\left[\sqrt{M^2-1}\right] \tag{B.4}$$

$$\theta = \nu(M_2) - \nu(M_1) \tag{B.5}$$

- **Relation between downstream and upstream pressures**

$$p_2 = \frac{p_2}{p_{02}}\frac{p_{02}}{p_{01}}\frac{p_{01}}{p_1}p_1 \tag{B.6}$$

Where:

$$\frac{p_{02}}{p_{01}} = 1$$

because the total pressure is conserved.

- **Ratio between total and static pressure**

$$\frac{p_0}{p} = \left(1 + \frac{\gamma-1}{2}M^2\right)^{\frac{\gamma}{\gamma-1}} \tag{B.7}$$

Bibliography

[1] T. Lampl, T. Wolf, M. Hornung, *"Preliminary Design of Advanced Flight Control System Architectures for Commercial Transport Aircraft"*, Aerospace Europe, 6th CEAS Conference, 2017.

[2] R. Fusaro, D. Ferretto, N. Viola, *"Flight Control System Design and Sizing Methodology for hypersonic cruiser"*, Politecnico di Torino, Turin, 10129, Italy.

[3] C. C. Coleman, F. A. Faruqi, *"On Stability and Control of Hypersonic Vehicles"*, Defence Science and Technology Organisation, DSTO-TR-2358, 2009.

[4] https://www.h2020-stratofly.eu/ (Accessed 24/10/2022)

[5] https://www.h2020moreandless.eu/project/ (Accessed 24/10/2022)

[6] N. Viola, R. Fusaro, D. Ferretto, O. Gori, M. Marini, P. Roncioni, B. O. Cakir, A. C. Ispir, B. H. Saracoglu, *"Hypersonic aircraft and mission concept re-design to move from Mach 8 to Mah 5 operations"*, 33rd Congress of the international Council of the Aeronautical Sciences, Stockholm, SE, 2022.

[7] N. Viola, P. Roncioni, O. Gori, R. Fusaro, *"Aerodynamic Characterization of Hypersonic Transportation Systems and Its Impact on Mission Analysis"*, Energies 2021, 14, 3580. https://doi.org/ 10.3390/en14123580

[8] P. Roncioni, M. Marini, *"Stratospheric Flying Opportunities for High-Speed Propulsion Concepts"*, D33-WP3.4 Final Report: CFD-based Aero-Propulsive Database, 2021.

[9] M. H Sadraey, *"Aircraft Design, a Systems Engineering Approach"*, John Wiley & Sons, Ltd. 2013.

[10] O. Gori, *"Simplified models for the preliminary aerodynamic characterization of high-speed vehicles to support mission analysis"*, 33rd Congress of the international Council of the Aeronautical Sciences, Stockholm, SE, 2022.

[11] L. J. Williams, *"Estimated aerodynamics of all-body hypersonic aircraft configurations"*, National Aeronautics and Space Administration, Washington, D.C., USA, 1971.

[12] G. Qiao, G. Liu, Z. Shi, Y. Wang, S. Ma, T. C Lim, *"A review of electromechanical actuators for More/All Electric aircraft systems"*, Journal of Mechanical Engineering Science, December 2017.

[13] *"Supersonic and Hypersonic Aircraft Market - A Global and Regional Analysis: Focus on Application, Subsystem, Speed Regime, and Country - Analysis and Forecast, 2022-2032"*. November 2022.

[14] Y. Sun, H. Smith, *"Review and prospect of supersonic business jet design"*. Progress in Aerospace Sciences, December 2016.

[15] https://www.spikeaerospace.com/s-512-supersonic-jet/ (Accessed 18/03/2023)

[16] https://boomsupersonic.com/overture (Accessed 18/03/2023)

[17] E. H. Hirschel, C. Weiland, *"Selected Aero-thermodynamic Design Problems of Hypersonic Flight Vehicles"*. Springer-Verlag Berlin Heidelberg (2009).

[18] S. L. Chernyshev, S. V. Lyapunov, A. V. Wolkov, *"Modern problems of aircraft aerodynamics"*. Chernyshev et al. Advances in Aerodynamics, (2019).

[19] F. Ding, J. Liu, C. Shen, Z. Liu, S. Chen, X. Fu, *"An overview of research on waverider design methodology"*. Acta Astronautica, August 2017.

[20] S. Matthes, D. S. Lee, R. R. De Leon, L. Lim, B. Owen, A. Skowron, R. N. Thor, E. Terrenoire, *"Review: Effects of Supersonic Aviation on Ozone and Climate"*. Aerospace, 2022.

[21] D. J. Maglieri, K. J. Plotkin, *"Sonic Boom"*. Aeroacoustics of Flight Vehicles: Theory and Practice: Volume 1: Noise Sources (1991).

Ringraziamenti

Vorrei dedicare questo piccolo spazio a chi ha contribuito alla realizzazione di questo elaborato. Prima di tutto, vorrei ringraziare i professori D. Ferretto, N. Viola e R. Fusaro che mi hanno proposto e dato la possibilità di trattare l'argomento di questa tesi.

Un ringraziamento particolare va al mio relatore D. Ferretto, che è stato sempre molto gentile e disponibile e mi ha seguito in tutte le fasi di questo lavoro dandomi sempre utili suggerimenti.

Vorrei ringraziare anche il dottorando O. Gori che è stato di grande aiuto soprattutto nella parte relativa alla caratterizzazione aerodinamica.

Infine, vorrei ringraziare delle persone che non hanno contribuito alla realizzazione di questa tesi ma che sono state comunque fondamentali, in primis i miei genitori a cui devo praticamente tutto, mia sorella e le mie amiche Alessia e Anna.